Kinesin-directed secretion of basement membrane proteins to a subdomain of the basolateral surface in *Drosophila* epithelial cells

Highlights

- A kinesin-3 and a kinesin-1 are required for normal BM assembly

- Kinesins move Rab10+ BM vesicles on microtubules polarized along two axes

- Transport biases BM exocytosis to basal subregions of the basolateral membrane

- Loss of kinesins creates ectopic BM networks that disrupt tissue architecture

Authors

Allison L. Zajac, Sally Horne-Badovinac

Correspondence

shorne@uchicago.edu

In brief

Zajac and Horne-Badovinac examine how basement membrane (BM) proteins are targeted to basal cellular regions for secretion in the context of the *Drosophila* follicular epithelium. They show that kinesin-based transport of Rab10+ BM secretory vesicles along polarized microtubules ensures that the BM network forms solely at the basal surface.

Article

Kinesin-directed secretion of basement membrane proteins to a subdomain of the basolateral surface in *Drosophila* epithelial cells

Allison L. Zajac[1] and Sally Horne-Badovinac[1,2,3,*]

[1]Department of Molecular Genetics and Cell Biology, The University of Chicago, 920 East 58th Street, Chicago, IL 60637, USA
[2]Twitter: @SHBLab
[3]Lead contact
*Correspondence: shorne@uchicago.edu
https://doi.org/10.1016/j.cub.2021.12.025

SUMMARY

Epithelial tissues are lined with a sheet-like basement membrane (BM) extracellular matrix at their basal surfaces that plays essential roles in adhesion and signaling. BMs also provide mechanical support to guide morphogenesis. Despite their importance, we know little about how epithelial cells secrete and assemble BMs during development. BM proteins are sorted into a basolateral secretory pathway distinct from other basolateral proteins. Because BM proteins self-assemble into networks, and the BM lines only a small portion of the basolateral domain, we hypothesized that the site of BM protein secretion might be tightly controlled. Using the *Drosophila* follicular epithelium, we show that kinesin-3 and kinesin-1 motors work together to define this secretion site. Similar to all epithelia, the follicle cells have polarized microtubules (MTs) along their apical-basal axes. These cells collectively migrate, and they also have polarized MTs along the migratory axis at their basal surfaces. We find follicle cell MTs form one interconnected network, which allows kinesins to transport Rab10+ BM secretory vesicles both basally and to the trailing edge of each cell. This positions them near the basal surface and the basal-most region of the lateral domain for exocytosis. When kinesin transport is disrupted, the site of BM protein secretion is expanded, and ectopic BM networks form between cells that impede migration and disrupt tissue architecture. These results show how epithelial cells can define a subdomain on their basolateral surface through MT-based transport and highlight the importance of controlling the exocytic site of network-forming proteins.

INTRODUCTION

The basement membrane (BM) is a sheet-like extracellular matrix present in most organs that plays essential roles in tissue development and physiology.[1,2] BMs provide attachment sites for cells, are a reservoir of growth factors, and mechanically shape tissues. The main structural components of the BM are type IV collagen (Col IV), laminin, heparan sulfate proteoglycans such as perlecan, and nidogen/entactin, which complex with many other proteins.[3] Defects in BM assembly underlie muscular dystrophy, nephropathy, skin blistering, vision problems, and stroke.[4–7] Despite the ubiquity of BMs and their clear importance, we know little about how BM proteins are secreted, and ultimately assembled, in the correct place within a tissue.

In this study, we investigate how a BM is built at the basal surface of an epithelium. BM proteins can be secreted from other tissues and/or produced by the epithelial cells; we focus on epithelial-cell-produced BMs. Epithelial cells generate and maintain their polarized membrane domains in part through sorting newly made proteins into apically or basolaterally directed secretory pathways.[8] Basolateral proteins are generally thought to be secreted through an apical region of the lateral membrane where Par-3 localizes the exocyst vesicle tethering complex,[9–11] or more uniformly along the lateral domain.[12,13] BM proteins

have unique sorting requirements relative to other basolateral proteins,[14–16] suggesting that they travel in a distinct secretory compartment. Since BM proteins form insoluble networks, their secretion site may also differ by being closer to the basal surface to prevent ectopic network formation.

One potential mechanism to bias BM protein secretion basally is suggested by the organization of microtubules (MTs) in epithelial cells. MT minus ends are anchored apically and plus ends grow toward the basal surface (Figure 1A),[17–22] suggesting that MTs could serve as tracks for plus-end-directed kinesin motors to transport BM-protein-filled secretory vesicles (BM vesicles) and bias their secretion near the BM. MT motors transport many apical proteins, but whether they transport basolateral cargoes like BM proteins is unknown.[8]

Much of what is known about the polarized secretion of BM proteins comes from studies of the follicular epithelium of *Drosophila*. This somatic epithelium surrounds a cluster of germ cells to form an ovarian follicle (egg chamber) that will produce one egg (Figure 1A).[23] Two small GTPases, Rab10 and Rab8, are required to sort BM proteins into a basolaterally directed trafficking route.[24–27] This allows follicle cells to build a BM on the egg chamber's outer surface that promotes tissue elongation (Figures 1B, 1C, and S1A).[27–30] The location where secretion occurs in this epithelium is thought to impact BM
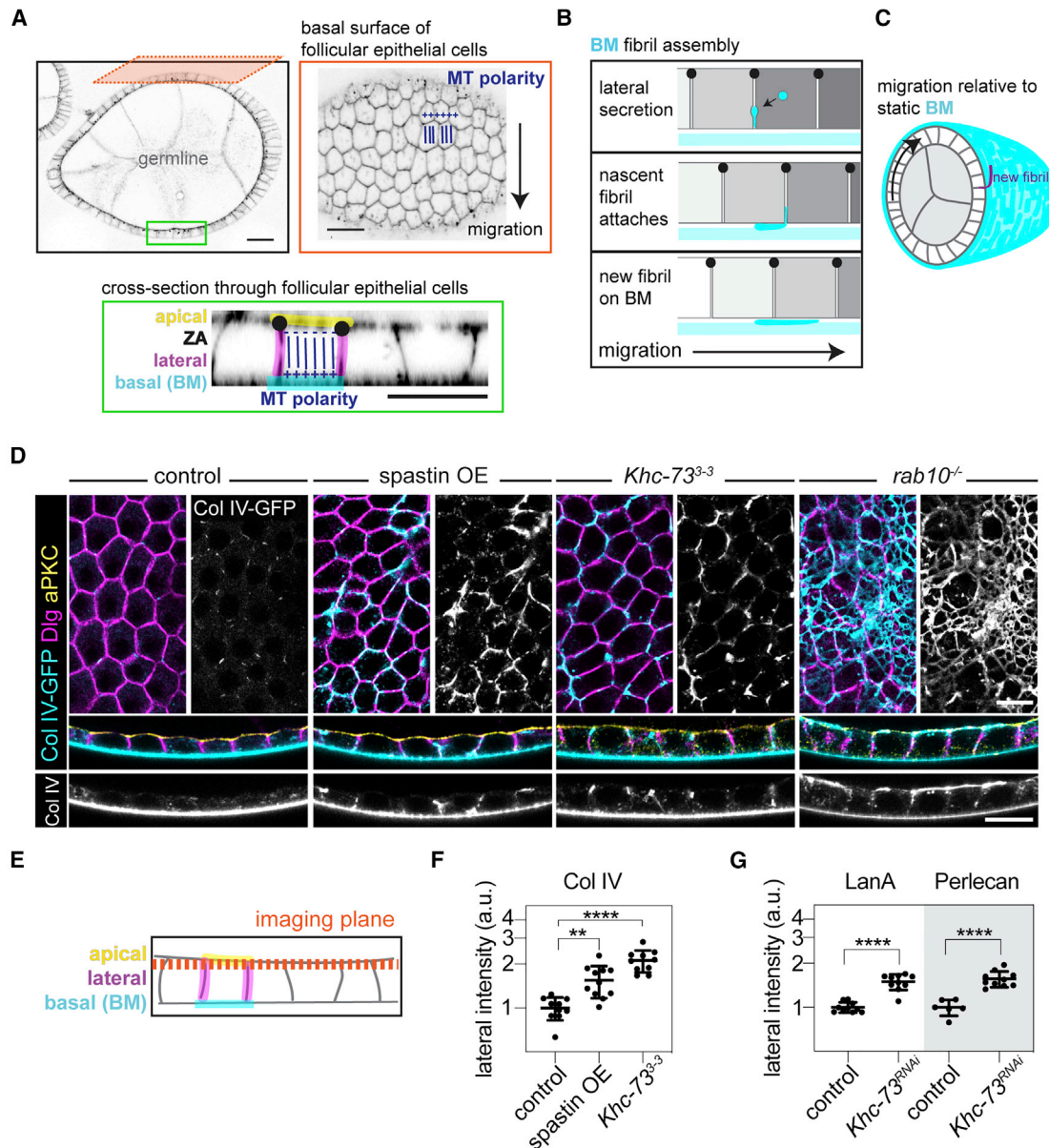
Figure 1. Khc-73 and MTs are required for polarized BM protein secretion

(A) Images of an egg chamber stained with CellMask. Green box highlights MT polarity along the apical-basal axis (ZA, zonulae adherentes). Orange box highlights MT polarity at the basal surface along the migratory axis.

(B and C) Illustrations of how BM fibrils form through lateral secretion and epithelial migration. Apical-basal axis of the epithelium (B). Transverse section through an egg chamber (C).

(D and E) Images of ectopic Col IV-GFP in epithelia of indicated genotypes (D). Top panels are planes through lateral domains that capture some of the apical surface due to tissue curvature, as diagrammed in (E). Bottom panels are cross-sections. Anti-Dlg (lateral domains). Anti-aPKC (apical domains, cross-sections only).

(F) Quantification of Col IV-GFP at lateral surfaces from (D). Ordinary one-way ANOVA with Dunnett's multiple comparisons test, $**p < 0.01$, $****p < 0.0001$. In order on graph, n = 10,11,10 egg chambers.

(G) Quantification of LanA and perlecan at lateral surfaces in control and $Khc-73^{RNAi}$ epithelia. Unpaired t test, $****p < 0.0001$. In order on graph, n = 10,10,6,10 egg chambers.

Stage 8. Data represent mean ± SD on a log scale. Scale bars, (A) 20 μm, all others 10 μm. See also Figures S1–S3 and Video S1.

structure. Some BM proteins are secreted laterally where they form fibrils in the intercellular space (Figure 1B).[27] Follicle cells collectively migrate along the BM,[29] which allows these fibrils to attach to the BM and be drawn out onto the BM as cells

migrate away from this anchor point (Figures 1B and 1C; Video S1).[27] In addition to the polarized MTs running along the apical-basal axis, MTs are also polarized along the basal surface of the follicle cells where they play a role in collective

migration.[31,32] The role of MT polarity along either axis in determining the secretion site of BM proteins is unknown.

Here, we show that kinesin-based transport biases the site of BM protein secretion to a basal subregion of the basolateral membrane. Our data suggest that the kinesin-3 motor, Khc-73, and the kinesin-1 motor, Khc, co-transport Rab10+ BM-protein-filled vesicles on MTs running along the apical-basal and migratory axes to their secretion site near the basal surface. When this transport is reduced, some BM proteins are mis-secreted through more apical regions of the lateral membrane and form ectopic networks between cells that disrupt tissue architecture. These results introduce a new transport step in the BM protein secretion pathway and highlight the importance of controlling the sub-cellular exocytic site of network-forming proteins.

RESULTS

Khc-73 biases BM protein secretion to basal regions

We hypothesized that BM vesicles are transported toward the basal surface by kinesins along the polarized MT network. As a first test of this hypothesis, we depleted MTs by overexpressing the MT-severing protein spastin,[33] and visualized the BM using a functional, endogenously GFP-tagged α2 chain of type IV collagen (Col IV-GFP).[34] In control cells, Col IV-GFP localizes to the BM, with only small Col IV-GFP puncta along lateral surfaces (Figures 1D–1F). In cells depleted of MTs, lateral Col IV-GFP increases (Figures 1D–1F and S1B). Therefore, MTs bias Col IV accumulation to basal cellular regions.

We performed an RNAi-based screen of *Drosophila* kinesins and identified the kinesin-3, Khc-73, as a candidate transport motor for BM vesicles. We used CRISPR to generate an allele, *Khc-73³⁻³*, which has an early stop codon in the motor domain (Figure S1C; STAR Methods). *Khc-73³⁻³* cells have ectopic Col IV-GFP along lateral surfaces, similar to cells overexpressing spastin (Figures 1D–1F). Placing the *Khc-73³⁻³* allele in *trans* to the *Khc-73¹⁴⁹* allele[35] also causes ectopic lateral Col IV-GFP (Figures S1D and S1E), confirming that mutation of Khc-73 causes this defect. Khc-73 loss similarly affects two other BM proteins, laminin and perlecan (Figure 1G). We know ectopic Col IV-GFP is extracellular because it is accessible to anti-GFP nanobodies in non-permeabilized tissue (Figure S1F). Therefore, BM proteins are secreted from *Khc-73³⁻³* cells but accumulate in the wrong location.

The ectopic lateral BM protein accumulation in *Khc-73³⁻³* epithelia differs from the mis-sorting of BM proteins into an apical secretory pathway caused by loss of previously identified regulators of BM protein secretion.[24–27,36] For example, loss of Rab10 causes an apical web-like network of Col IV-GFP, with minor Col IV-GFP along lateral surfaces (Figure 1D).[25] In contrast, most ectopic Col IV-GFP in *Khc-73³⁻³* cells is below the zonulae adherentes (ZAs), which demarcate lateral and apical domains (Figures 2A and 2B); there are not occluding junctions present while the BM is being made.[37–39] During the developmental stages when Col IV synthesis is high, ectopic extracellular Col IV-GFP accumulates all along the lateral domain in *Khc-73³⁻³* cells (Figures 2C–2E). As Col IV secretion ends, the ectopic Col IV becomes biased to an apical (upper) region of the lateral domain (Figure 2A), likely

due to the movement of fibrils onto the BM that clears the basal (lower) regions of the lateral domain (Figure 2F). The lateral ectopic Col IV-GFP in *Khc-73³⁻³* tissue suggests that BM proteins are sorted into a basolateral pathway, but their secretion site expands to upper regions of the lateral membrane (Figure 2F).

Our investigation of Khc-73 was motivated by the hypothesis that it transports vesicular cargo, similar to many kinesin-3 family members.[40] However, kinesins play other roles in epithelial cells.[41] Apical-basal cortical polarity, polarized localization of transmembrane proteins, localization of Col-IV-encoding mRNAs, and MT organization are all normal in *Khc-73³⁻³* cells (Figures 1D, S2A–S2D, and S3A–S3G). These data suggest that epithelial cell organization remains intact in Khc-73's absence, supporting the idea that Khc-73 affects BM protein secretion through vesicular transport.

Altogether, these data suggest that Khc-73 biases BM protein secretion basally to ensure the BM forms in the correct location.

Khc-73 transports Rab10+ BM protein secretory compartments to basal regions

To determine how Khc-73 biases the site of BM protein secretion, we examined the secretory pathway. Normally, we only detect intracellular Col IV-GFP in the endoplasmic reticulum (ER), preventing us from following Col IV-GFP in secretory vesicles (Figure S4A). Rabs define different membrane compartments by recruiting effectors that carry out the sorting, transport, and fusion steps of membrane trafficking.[42] As an alternate marker of BM vesicles, we used Rab10, which is required for polarized BM secretion[25] and is known to direct secretory transport in other systems.[43–46] YFP-Rab10 localizes near the Golgi, which in *Drosophila* is distributed among all ER exit sites (ERES) and is where BM vesicles likely form (Figures 3A and 3B).[25] YFP-Rab10 also labels punctate/tubular compartments along the basal surface that preferentially accumulate at the trailing edge of each migrating cell (Figure 3A).[25] As these compartments are away from the Golgi, they likely represent secretory intermediates. Rab10 also interacts with kinesin motors, including the human homolog of Khc-73.[47,48] Khc-73-GFP is enriched with Rab10 at basal trailing edges (Figure 3C), suggesting that Khc-73 may transport Rab10+ secretory compartments from the Golgi to this location.

To ask how kinesin transport mediates Rab10's localization, we examined the organization of MTs. In 3D image volumes taken near the basal surface, the apical-basal MTs (Figure 3D) and the basal MTs (Figure 3E) appear connected. Bundled MTs lying along the basal surface bend at leading edges and integrate with the apical-basal MTs (Figures 3E and 3F; Video S2). We cannot resolve individual MTs to know whether these bundles contain individual bent MTs or whether there are two independent MT networks that intersect at the front of the cell (Figure 3F). However, proteins commonly found at MT-organizing centers (MTOCs), such as the minus-end-binding protein Patronin and a component of the γ-tubulin ring complex, γ-Tubulin at 23C (γTub23C), are predominantly enriched near the apical surface, which was shown previously for Patronin (Figures S4B–S4G).[21,22] These results are most consistent with follicle cells having only one dominant apical MTOC, but since there is diffuse Patronin and γTub23C filling cells,
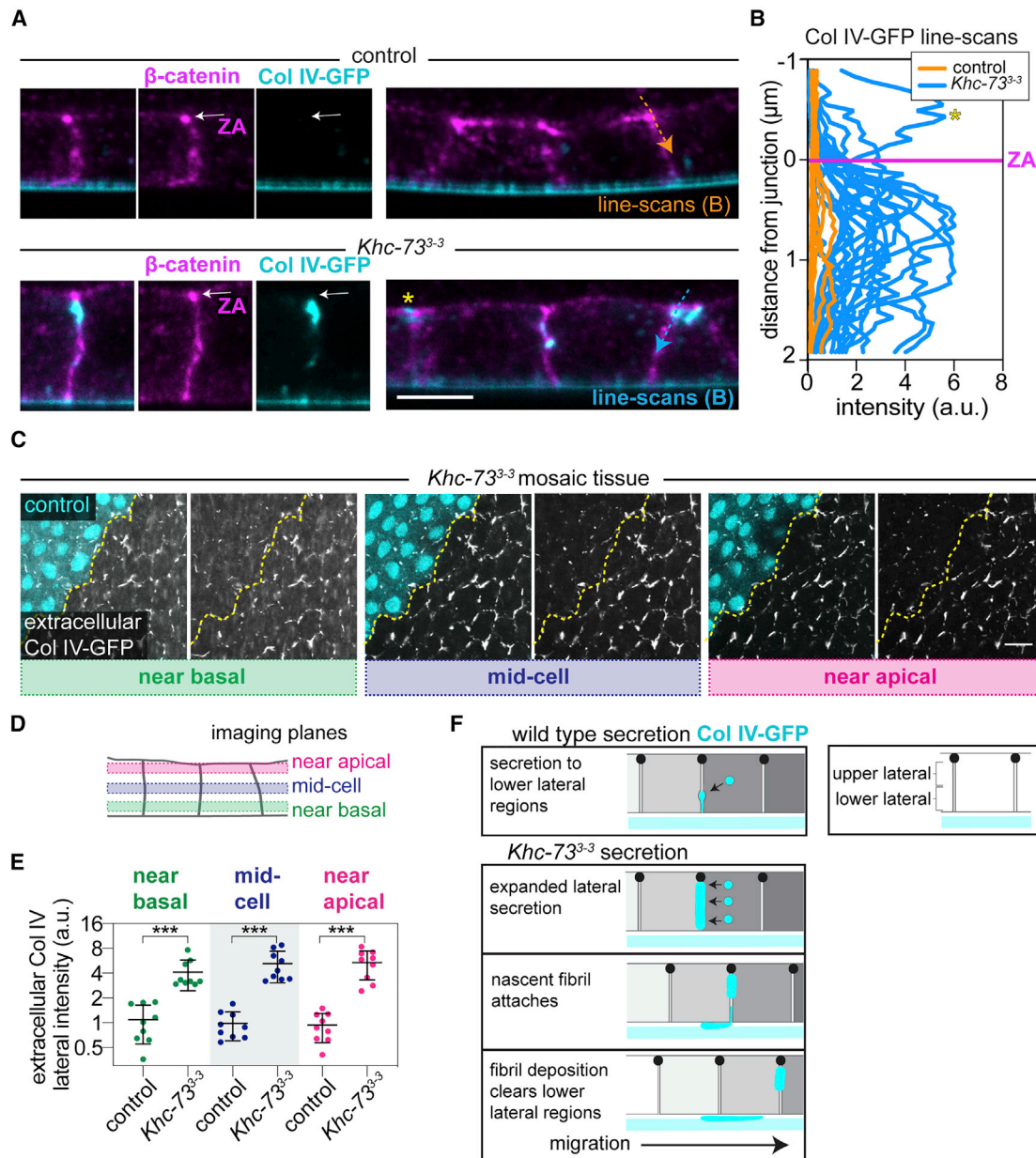
Figure 2. Col IV accumulates all along the lateral domain in *Khc-73³⁻³* cells

(A) Images of lateral Col IV-GFP in control and *Khc-73³⁻³* epithelia relative to ZA (white arrows). Dotted arrows indicate site of intensity line scans in (B).

(B) Graph of Col IV-GFP fluorescence intensity along cell-cell interfaces as indicated in (A). Col IV-GFP line scans were aligned to peak β-cat signal at the ZA (magenta line). Asterisk highlights the example of Col IV-GFP apical to the ZA from (A). n = 18 control, 20 *Khc-73³⁻³*.

(C and D) Images of extracellular Col IV-GFP in *Khc-73³⁻³* mosaic tissue at three z planes through the lateral domain (C), diagrammed in (D). Line demarcates control and *Khc-73³⁻³* cells. Extracellular Col IV-GFP is highlighted by staining non-permeabilized tissue with an anti-GFP nanobody (Figure S1F).

(E) Quantification of extracellular Col IV-GFP in (C), showing increased lateral accumulation in *Khc-73³⁻³* cells at all three z planes. Data represent mean ± SD on a log scale. Paired t tests, ***p < 0.001. n = 9 egg chambers.

(F) Model for how Khc-73 loss causes lateral Col IV accumulation, which persists mainly in the upper region of the lateral domain.

Stage 8 (A and B). Stage 7 (C and E). Scale bars, 5 μm (A), 10 μm (B). See also Figure S1.

---

there may also be MT minus ends distributed more sparsely throughout cells.

Based on the polarity of MTs along the apical-basal and migration axes (Figures S4H and S4I),[21,22,31,49] the 3D MT organization could allow plus-end-directed kinesin transport to concentrate Rab10+ compartments at basal trailing edges (Figure 3F). Indeed, YFP-Rab10+ puncta move rapidly along the basal MTs (Figure 3G; Video S3). Motile puncta enter the basal focal plane at leading edges where MT bundles also come into view (Figure 3G'; Video S3), suggesting that transport from more apical
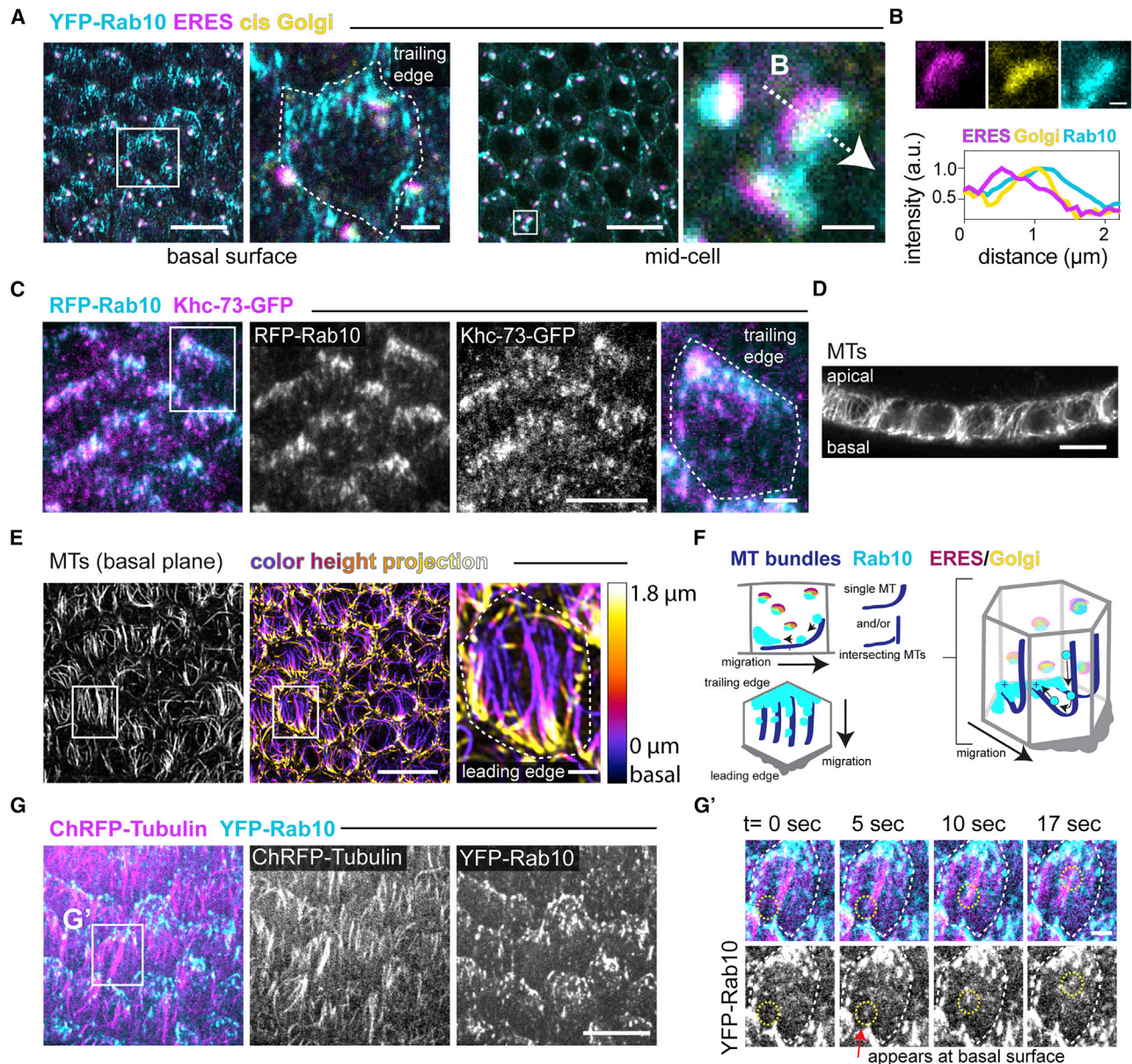
Figure 3. Rab10+ compartments move along MTs to basal trailing cell edges

(A and B) Images of UAS-YFP-Rab10 at the basal surface and mid-cell (A). The basal inset highlights one cell (outlined) with UAS-YFP-Rab10 at the trailing edge. The mid-cell inset shows UAS-YFP-Rab10 relative to the ERES protein Tango1 and the *cis* Golgi protein GM130, with single-channel examples and a line scan of example intensity profiles (B). Scale bars, 10 μm main panels, 2 μm basal inset, 1 μm ERES/Golgi inset (A), and 0.5 μm (B).

(C) Image of Khc-73-GFP (endogenous promoter) localizing to UAS-RFP-Rab10+ tubular compartments at basal trailing cell edges. Inset one cell (outlined).

(D and E) Images of MTs (anti-acetylated α-tubulin) aligned along the apical-basal axis in cross-section (D) and along the migratory axis at the basal surface (E, left). A color height projection (center) of the basal-most 1.8 μm of the epithelium shows that MT bundles at the cells' leading edges bend and extend apically. Inset is one cell (right, outlined).

(F) Illustrations of the 3D organization of Rab10+ compartments on MT bundles that bend near the basal leading cell edges, as viewed in cross-section, along the basal surface, or in a 3D cell. Only a few bent MTs/MT bundles are shown for clarity.

(G) Image from time-lapse showing that UAS-YFP-Rab10+ compartments move along basal MTs (UAS-ChRFP-α-tubulin). (G′) Montage of a YFP-Rab10+ punctum appearing in the basal focal plane and moving along a MT bundle from inset in (G).

Stage 7 (A–E). Stage 8 (G). Images oriented with migration down. Scale bars, 10 μm for main panels and 2 μm for cell insets, except as described in (A). See also Figure S4 and Videos S2 and S3.

regions to the basal surface occurs along these bent MTs, although we cannot resolve if this occurs in one smooth step. YFP-Rab10+ puncta move toward the trailing edge of cells ∼2-

fold more often than toward the leading edge (202/297 trajectories in 5 egg chambers), consistent with transport contributing to the trailing edge enrichment. EB1-GFP-positive comet growth is
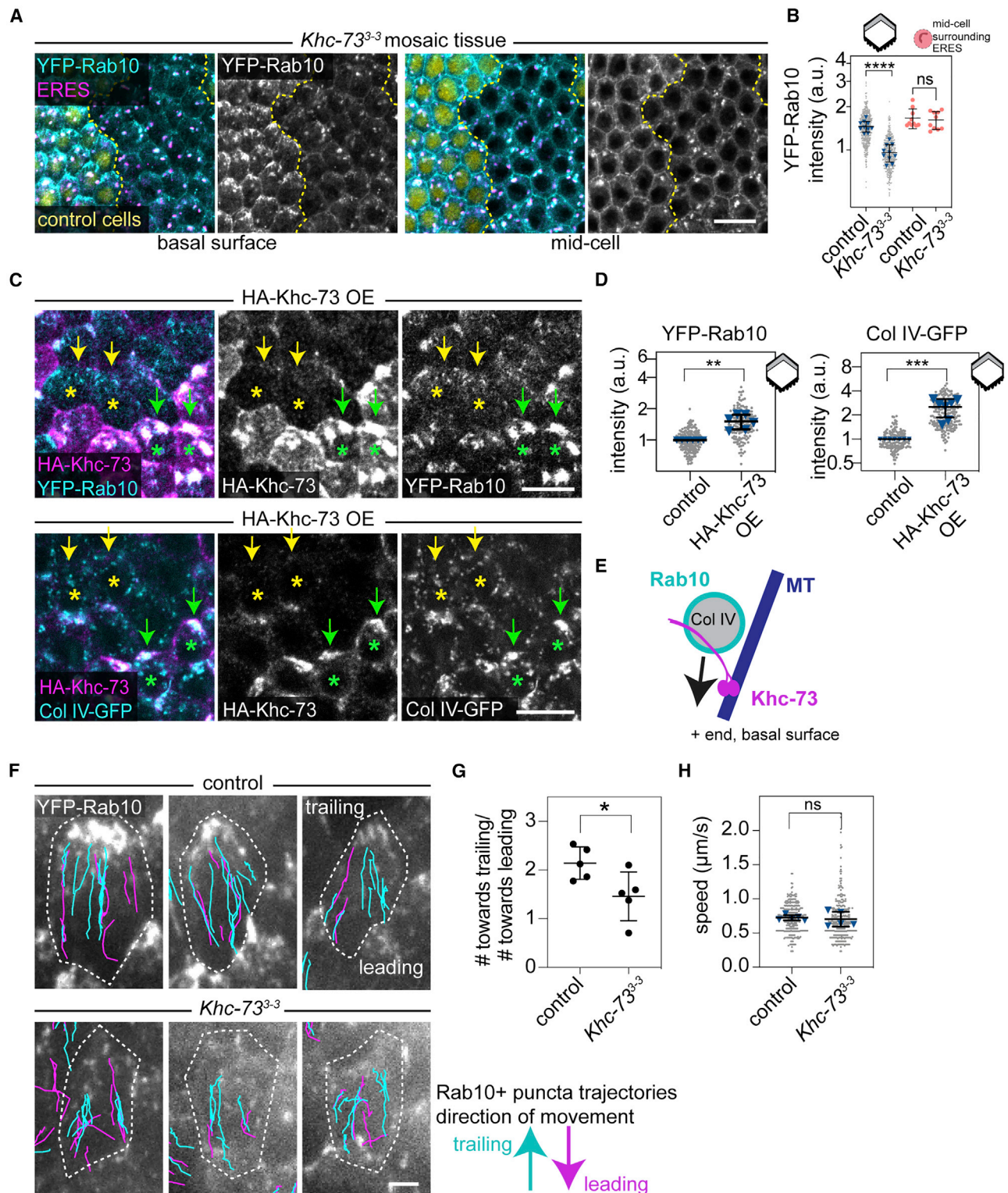
Figure 4. Khc-73 transports Rab10+ compartments to the basal trailing edges of cells

(A) Images of UAS-YFP-Rab10 and ERES (anti-Tango1) in $Khc-73^{3-3}$ mosaic tissue at the basal surface and mid-cell. Line demarcates control and $Khc-73^{3-3}$ cells.

(B) Quantification of the decrease in UAS-YFP-Rab10 levels at basal trailing cell edges (gray region of cell in cartoon) without a change near the ERES mid-cell (salmon) in $Khc-73^{3-3}$ cells. Gray dots represent individual cells and blue triangles represent egg chamber means. For basal surface: paired t test, ****$p < 0.0001$. n = 10 egg chambers, 544 control and 457 $Khc-73^{3-3}$ cells. For ERES: Wilcoxon matched-pairs signed-rank test; ns, $p > 0.05$. n = 10 egg chambers.

only ∼84% biased toward the trailing edge (Figure S4I; Video S5), consistent with previous work.[31] Therefore, the bidirectional movement of Rab10+ puncta may be due to kinesin-driven movement on the mixed polarity MTs and/or contributions from a minus-end-directed motor such as dynein. In conclusion, the bias in Rab10+ puncta movement is consistent with a role for MT motor transport of Rab10+ secretory vesicles to basal trailing cell edges.

Next, we asked if Khc-73 transports Rab10+ compartments basally. Loss of Khc-73 reduces YFP-Rab10 levels at basal trailing cell edges but does not increase its levels at the Golgi, suggesting that BM vesicles are not trapped there (Figures 4A and 4B). This result supports our finding that Khc-73 is not needed for BM protein secretion to occur, just to specify its location (Figures 2C–2F). Conversely, overexpressing Khc-73 increases YFP-Rab10 basally, where it forms large, aberrant foci (Figures 4C and 4D). We do not normally see Col IV-GFP colocalized with Rab10. However, Col IV-GFP is concentrated within the aberrant foci (Figures 4C and 4D), which suggests that they are clusters of trapped BM vesicles. Supporting this idea, the foci lack markers of the ER and Golgi (Figures S5A and S5B) and YFP-Rab10+ tubulovesicular structures move rapidly into and out of them (Video S4). These data show that Khc-73 is necessary for Rab10+ compartment localization to the basal surface and sufficient to alter the localization of Rab10+ and Col IV+ compartments when overexpressed.

Our observations that Rab10+ puncta move preferentially toward cellular regions enriched in growing MT plus ends, and that changes in Khc-73 expression affect the localization of both Rab10+ and Col IV+ compartments, strongly suggest that Khc-73 transports BM vesicles basally (Figure 4E).

Kinesin-1 works with Khc-73 to direct BM protein secretion basally

Khc-73 is the only motor whose individual knockdown perturbed Col IV secretion in our RNAi screen. However, the few YFP-Rab10+ puncta that reach the basal surface in Khc-73[3–3] tissue move at normal speeds (control: 0.72 ± 0.21 and Khc-73[3–3]: 0.71 ± 0.31 μm/s), although with less trailing edge bias (Figures 4F–4H; Video S5). Multiple kinesins often contribute to cargo transport.[50] Since kinesin-1 transports Rab10 in other contexts,[43] we investigated if kinesin-1 works with Khc-73 to transport Rab10+ BM vesicles.

Co-depletion of Khc-73 and kinesin-1's heavy chain, Khc, using RNAi caused higher accumulation of Col IV-GFP along lateral membranes than Khc-73[RNAi] alone (Figures 5A–5C). We confirmed that loss of Khc alone does not cause lateral Col IV-GFP accumulation using a null allele, Khc[27] (Figures S5C and S5D).[51] Co-depletion of Khc-73 and kinesin light chain (Klc), which often acts as a cargo adaptor for Khc,[52] similarly enhanced lateral Col IV-GFP accumulation (Figures 5A–5C). Interestingly, if we further deplete kinesin activity by combining Khc-73[3–3] with Khc[RNAi], the ectopic Col IV-GFP shifts to the apical surface (Figures 5A–5C). These dual kinesin depletions show that kinesin-1 works with Khc-73 to promote basally polarized BM protein secretion. Further, these results reveal that BM proteins can accumulate apically when both kinesins are strongly depleted, suggesting that more severe loss of plus-end-directed transport may redirect secretion apically, perhaps through dynein, or that kinesins also play an earlier role in basolateral sorting of BM proteins.

Next, we asked if Khc affects BM protein secretion by the same mechanism as Khc-73, transporting Rab10+ compartments toward the basal surface. First, cell organization is unaffected in Khc[RNAi] & Khc-73[3–3] cells, as the polarized localization of cortical and transmembrane proteins, Col IV-encoding mRNAs, and MTs all remain normal (Figures 5A and S6A–S6H). However, depletion of Khc in Khc-73[3–3] tissue shifts YFP-Rab10 from the basal surface to the apical surface relative to Khc-73[3–3]-only tissue (Figures 5D–5F). Therefore, we favor the model that Khc works with Khc-73 to transport Rab10+ BM vesicles to the basal surface (Figure 5G).

Multiple kinesins often work together, taking advantage of differences in their mechanochemical properties and preferences for MT modifications, to cooperatively transport cargo to the correct location.[53] To ask if Khc and Khc-73 make unique contributions to Rab10 transport, we compared how Rab10 localization changes when it is transported by only one of the two kinesins (Figure S7A). YFP-Rab10 is reduced at basal trailing edges in Khc-73[3–3] cells, where Khc is likely to be the dominant plus-end-directed motor (Figures 4A, 4B, and S7A). Surprisingly, this population of YFP-Rab10+ is instead increased in Khc[27] cells, where Khc-73 is likely to dominate (Figures 6A, 6B, and S7A). These experiments used one copy of endogenously labeled YFP-Rab10 to ensure that high Rab10 levels did not

(C) Images of YFP-Rab10 (endogenous, top) and Col IV-GFP (endogenous, bottom) in epithelia overexpressing UAS-HA-Khc-73 in patches of cells. YFP-Rab10 images are along basal surface. Col IV-GFP images are 1.5 μm above the basal surface to avoid signal from the BM. Yellow asterisks indicate "control" cells negative for HA-Khc-73 staining; yellow arrows point at the trailing cell edges. Green asterisks label HA-Khc-73 OE cells; green arrows point to foci at trailing cell edges.

(D) Quantification of the increase in YFP-Rab10 and Col IV-GFP in HA-Khc-73 OE cells at basal trailing cell edges (gray region of cell in cartoon). Gray dots represent individual cells and blue triangles represent egg chamber means. One-sample t tests compared with the theoretical ratio of 1, **p < 0.01, ***p < 0.001. For YFP-Rab10, n = 6 egg chambers, 199 "control," and 161 HA-Khc-73 OE cells. For Col IV-GFP, n = 7 egg chambers, 149 "control," and 214 HA-Khc-73 OE cells.

(E) Model for how Khc-73 transports Rab10+ Col IV-filled secretory vesicles.

(F) Images of example cells (outlined) from frame one of a time-lapse of control and Khc-73[3–3] epithelia expressing UAS-YFP-Rab10. Trajectories of UAS-YFP-Rab10+ puncta are overlaid on images and color-coded for direction.

(G) Quantification of movement of UAS-YFP-Rab10+ puncta toward leading or trailing edges in control and Khc-73[3–3] epithelia from (F). Unpaired t test, *p < 0.05. n = 5 egg chambers, 297 runs in control, and 305 runs in Khc-73[3–3] egg chambers. Control data also used in the text of Results section.

(H) Distribution of speeds of UAS-YFP-Rab10+ puncta in control and Khc73[3–3] epithelia at the basal surface. Gray dots represent individual runs, and blue triangles represent egg chamber means. Unpaired t test; ns, p > 0.05. n = 5 egg chambers, 297 runs in control, and 305 runs in Khc-73[3–3] egg chambers.

Stage 7. Images oriented with migration down. Data represent mean ± SD. Statistics were performed on egg chamber mean values. Data in (B) and (D) plotted on log scale. Scale bars, 10 μm (A and C), 2 μm (F). See also Figures S5A and S5B and Videos S4 and S5.
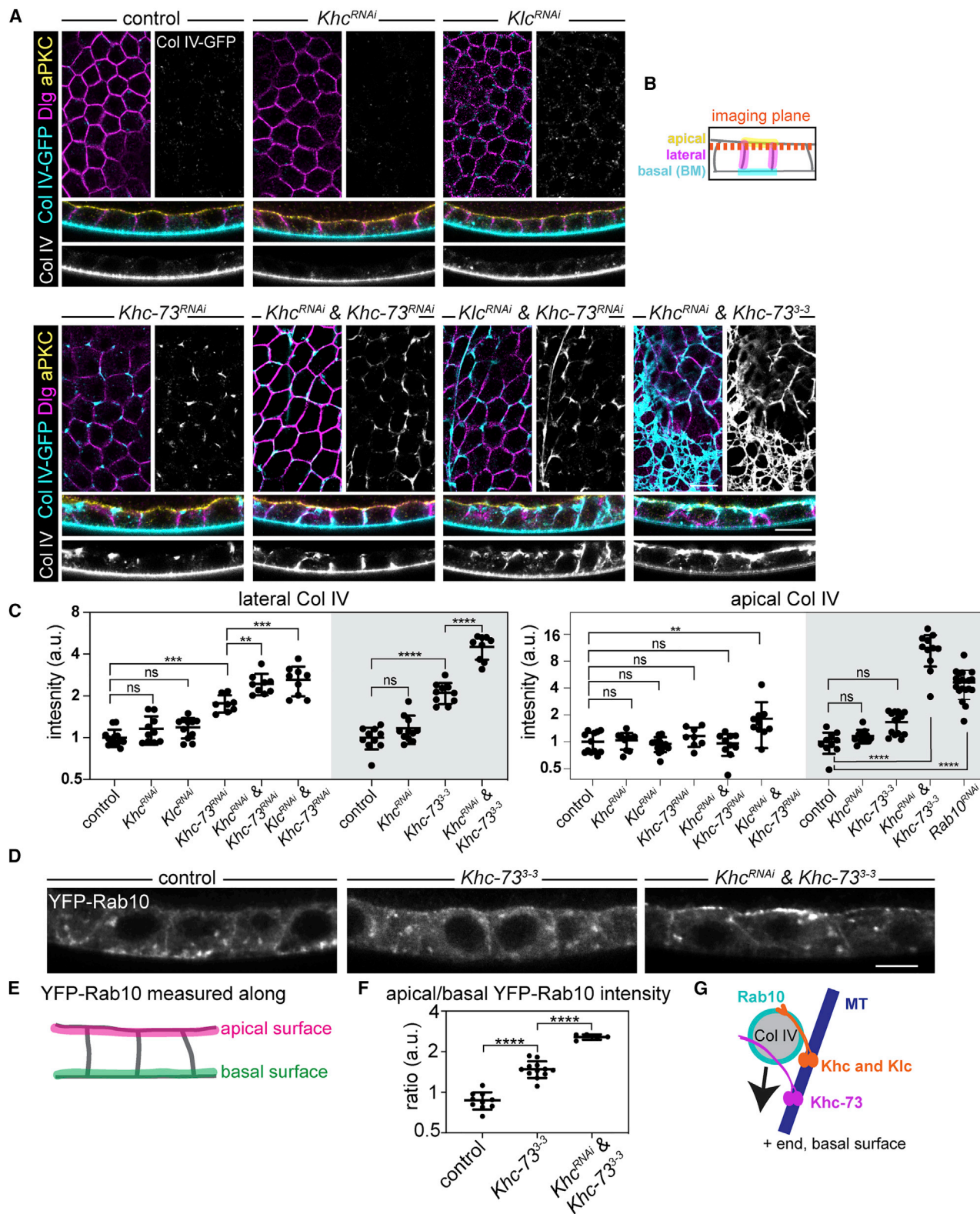
Figure 5. The kinesin-1 Khc works with Khc-73 to direct polarized BM protein secretion

(A and B) Images showing ectopic Col IV-GFP in epithelia of indicated genotypes (A). Top panels are planes through lateral domains that capture some of the apical surface due to tissue curvature, as diagrammed in (B). Bottom panels are cross-sections. Anti-Dlg (lateral domains). Anti-aPKC (apical domains, cross-sections only).

(legend continued on next page)

affect the results. Although Khc can rearrange MTs by binding a second MT with its tail domain and sliding MTs relative to each other,[54] MTs remain aligned in Khc^{27} cells (Figures S7B–S7D). Additionally, a mutation that selectively impairs Khc's ability to slide MTs[55] does not affect YFP-Rab10 (Figures 6A and 6B), indicating that Khc's cargo transport activity plays the key role in Rab10 localization.

We hypothesized that increased Khc-73 activity compensates for loss of Khc and causes changes to Rab10+ compartment localization. Supporting this idea, Khc-73-GFP is increased at the basal trailing edges of Khc^{27} cells (Figures 6C and 6D). Additionally, Khc-73 overexpression causes accumulation of YFP-Rab10 in large foci at basal trailing edges that resemble those in Khc^{27} cells (Figures 4C, 4D, and S7A). These data imply that increased Khc-73 activity compensates for loss of Khc. However, increased reliance on Khc-73 causes additional Rab10+ compartment localization to basal trailing cell edges (Figure S7A), suggesting that Khc is needed to achieve the normal distribution of Rab10+ compartments.

Overall, our data suggest that Khc works with Khc-73 to prevent apical secretion and transport Rab10+ BM vesicles to basal trailing cell edges to bias the site of BM protein secretion (Figure S7E).

Intercellular BM protein networks disrupt tissue architecture

Finally, we investigated how changing the secretion site of BM proteins impacts the structure of the BM and the cells migrating along it. Col IV-GFP levels are normal within the BM in all genotypes where kinesins are reduced, except the condition that causes apical accumulation, Khc^{RNAi} & $Khc-73^{3-3}$ (Figures 7A and 7B). However, the structure of the BM changes, with increased Col IV-GFP incorporated into fibrils in $Khc-73^{3-3}$ BMs and Khc^{RNAi} & $Khc-73^{RNAi}$ BMs (Figures 7A and 7D). Therefore, although Col IV is initially mis-secreted all along the lateral membrane, much of this protein eventually moves onto the BM as fibrils (Figure 2F). We previously proposed that the relative proportion of BM proteins secreted to lateral versus basal membranes determined the size of BM fibrils.[27] Decreased kinesin transport seems to shift this balance.

The kinesin mutant conditions also have persistent lateral accumulations of Col IV. To understand how this Col IV is organized relative to cells, we made 3D projections of the non-BM Col IV-GFP. In the apical secretion condition, Khc^{RNAi} & $Khc-73^{3-3}$, Col IV-GFP lies above the apical surface (Figure 7C). In conditions that cause lateral secretion, Col IV-GFP forms an intercellular network that spans multiple cells (Figure 7C) and can connect to the underlying BM. As follicle cells are collectively migrating along the BM, these connections seem to impede cell movement. This is best illustrated in the milder condition, $Khc-73^{3-3}$, where only a few, isolated Col IV-GFP cables run between cells and anchor to the BM at one end (Figure 7E, white arrows; Video S6). The hexagonal packing of follicle cells is disrupted near these cables and several nuclei are highly deformed (Figure 7E, green arrows and inset). Some cells are likely forced to squeeze through the intercellular network of Col IV-GFP cables during migration, causing this nuclear deformation. This drastic effect on cells from only the relatively small fraction of Col IV within these cables highlights the importance of tightly controlling the secretion site of network-forming proteins.

DISCUSSION

This work provides the first mechanistic insight into how the secretion site of BM proteins is controlled in an epithelium. We identified a kinesin-3 motor, Khc-73, and a kinesin-1 motor, Khc, required for this process. When these motors are depleted, BM proteins form ectopic networks away from the basal surface that disrupt tissue architecture. Reducing kinesin levels also alters the localization and movement of Rab10+ BM-protein-filled secretory compartments. We propose that these kinesins transport BM vesicles basally to bias the site of BM protein secretion and facilitate formation of a single BM sheet at the basal surface (Figure S7E).

Polarized secretory pathways in epithelial cells are typically grouped into two destinations, apical and basolateral.[8] Here, we find that kinesin transport along MTs imparts additional spatial regulation by targeting BM protein secretion to a basal subregion of the basolateral domain in follicle cells. We further find that the apical-basal MT network is connected to another polarized MT network that runs along the basal surface. MTOC-associated proteins are predominately apical, suggesting that the basal MTs may simply be a reorganization of the apical-basal network where it contacts the basal surface; however, future work is required to fully define 3D MT organization. The connection between the two MT networks likely explains why Rab10+ compartments transported by kinesins are enriched not only basally, but also at the trailing edges of migrating follicle cells. Here, BM secretory vesicles are positioned to fuse with the lower lateral membrane, which would restrict BM fibril formation near the basal surface for easy transfer to the BM during migration (Figure S7E). Network-forming proteins such as BM proteins may be especially reliant on spatial control of secretion to ensure they assemble in the correction location. However, other cargoes are also targeted to a basal region of the basolateral


(C) Quantification of ectopic Col IV-GFP at lateral edges in the plane illustrated in (B) on left and in a line scan along the apical domain on right. The control and $Khc-73^{3-3}$ data in the gray region of graph are reproduced from Figure 1F. Data represent mean ± SD plotted on a log scale. Lateral Col IV: ordinary one-way ANOVA with Šídák's multiple comparisons test; ns, p > 0.05; **p < 0.001, ***p < 0.0005, ****p < 0.0001. In order on graph, n = 13, 10, 11, 8, 9, 9, 10, 11, 10, and 9 egg chambers. Apical Col IV: ordinary one-way ANOVA with Dunn's multiple comparisons test; ns, p > 0.05; **p = 0.0041, ****p < 0.0001. In order on graph, n = 12, 10, 14, 8, 10, 10, 10, 12, 14, 11, and 19 egg chambers.

(D) Cross-sectional images through UAS-YFP-Rab10-expressing epithelia lacking Khc-73 only, or lacking Khc-73 and depleted of Khc.

(E and F) Quantification of the ratio of YFP-Rab10 intensity along the apical surface divided by the basal surface, as illustrated in (E), from images in (D). Graph showing Rab10 shifts to apical surface when kinesins are depleted (F). Data represent mean ± SD plotted on a log scale. Ordinary one-way ANOVA with Šídák's multiple comparisons test; ****p < 0.0001. In the order on graph, n = 10, 12, and 5 egg chambers.

(G) Model for two kinesins' role in transporting BM vesicles.

Stage 8. Scale bars, 10 μm (A) and 5 μm (D). See also Figures S5 and S6.
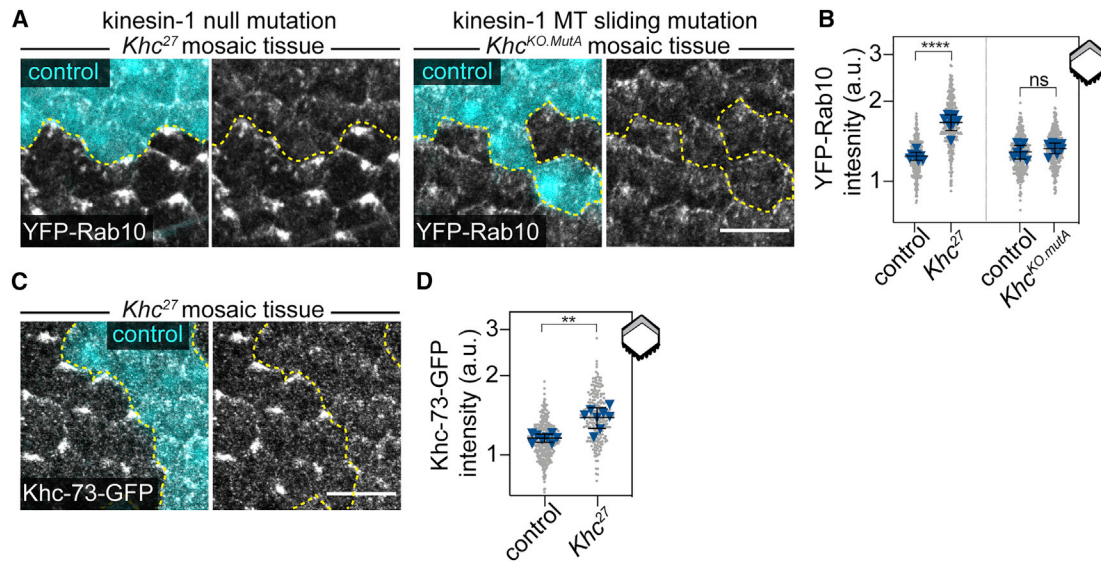
Figure 6. Khc and Khc-73 make distinct contributions to Rab10+ compartment localization at the basal surface

(A) Image of YFP-Rab10 (endogenous) along the basal surface in Khc^{27} and $Khc^{KO.mutA}$ mosaic tissues. Line demarcates control and mutant cells.

(B) Quantification of the increase in YFP-Rab10 (endogenous) at the basal trailing edge (gray region of cell in cartoon) of Khc^{27} cells, with no change in $Khc^{KO.mutA}$ cells. Gray dots represent individual cells and blue triangles represent egg chamber means. Paired t tests; ns, p > 0.05; ****p < 0.0001. For Khc^{27}, n = 8 egg chambers, 351 control, and 339 mutant cells. For $Khc^{KO.mutA}$, n = 8 egg chambers, 344 control, and 366 mutant cells.

(C) Image of Khc-73-GFP (endogenous promoter) along the basal surface in Khc^{27} mosaic tissue. Line demarcates control and Khc^{27} cells.

(D) Quantification of the increase in Khc-73-GFP (endogenous promoter) at the basal trailing edge (gray region of cell in cartoon) of Khc^{27} cells. Gray dots represent individual cells and blue triangles represent egg chamber means. Paired t test, **p < 0.01. n = 8 egg chambers, 372 control, and 245 Khc^{27} cells. Stage 7. Data represent mean ± SD plotted on a log scale. Statistics are on egg chamber means. Scale bars, 10 μm. See also Figure S7.

domain, as well as other defined sites like junctions and primary cilia,[10,56–58] which may indicate a broader role for MT transport and spatial control of secretion in epithelial cells.

Multiple kinesin motors often work together during vesicular transport, although their specific contributions, especially on native cargo,[59–61] are only beginning to be dissected. Khc-73 localizes to Rab10+ structures, and its loss alone causes BM defects, suggesting that it plays a major role in BM vesicle transport. However, additional loss of Khc enhances the severity of both the BM secretion and Rab10 localization defects, suggesting that both motors contribute to BM secretion. We favor the model that both kinesins associate with Rab10+ structures and take advantage of their different motor properties and preferences for MT modifications to cooperatively transport BM vesicles to the correct secretion site. Consistent with this model, human homologs of Khc-73 and Khc also work together during secretory transport in HeLa cells.[59] Loss of Khc alone has the opposite effect on Rab10 localization as loss of Khc-73. However, since Khc-73 overexpression disrupts Rab10 localization in a similar way, Khc-73 likely compensates for Khc loss and creates this increase. Kinesin-3 family motors like Khc-73 have high processivity and the ability to quickly rebind MTs, features that optimize them for long distance transport.[40,62,63] This may allow Khc-73 to bring more Rab10+ BM vesicles to the terminal plus ends of MTs when it acts in the absence of Khc. Alternatively, Khc-73 may have additional functions, such as the ability to tether vesicles at basal trailing edges, that differentiate it from Khc.

Kinesin-based transport likely integrates with other mechanisms to ensure BM proteins assemble into a single sheet. Integrins and the dystroglycan complex may influence where BM

networks assemble and could aid in post-secretion movements of BM proteins such as those required for BM fibril formation.[1,64] We previously showed that Col-IV-encoding mRNAs are enriched basally in follicle cells and proposed that local Col IV protein synthesis promotes polarized BM protein secretion.[25] Thus, kinesin-based transport of Rab10+ secretory vesicles may ensure that the subset of BM proteins that are synthesized away from the basal surface reach the correct secretion site and thereby maintain or refine the polarity established by basal Col IV synthesis. Kinesin-based transport of BM proteins may be particularly important in mammalian cells, where a single, apically localized Golgi apparatus creates an even bigger spatial problem for BM protein secretion.

Finally, this work demonstrates that tightly controlling the subcellular site of BM protein secretion is critical for BM formation and tissue architecture. We previously showed that targeting BM protein secretion to lateral surfaces alters the architecture of the follicular BM in a way that is beneficial for the tissue—it allows the formation of the BM fibrils necessary for normal egg chamber elongation.[27] However, it is now clear that BM protein secretion cannot occur anywhere along the lateral membrane, as secretion to the upper region of this domain causes BM protein networks to form between cells. Moreover, when these ectopic networks attach to the BM, they act as anchors that locally impede collective migration, distorting cell shapes to such an extent that even nuclei are deformed. We imagine that the formation of ectopic BM networks between cells would be detrimental to any epithelium undergoing cellular rearrangements, either during development or homeostatic tissue turnover.[1,65] We propose that kinesin-based transport of BM
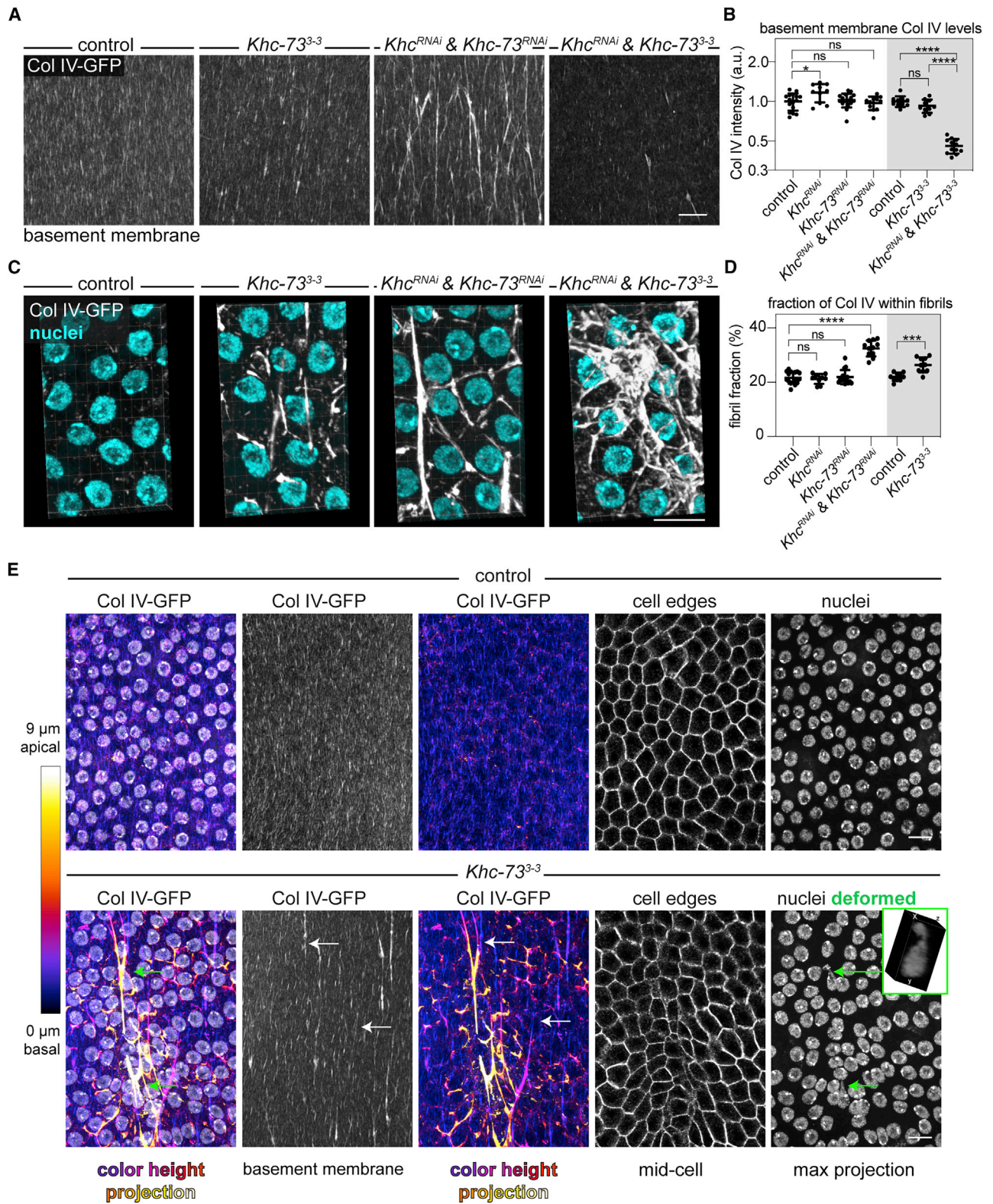
Figure 7. Intercellular BM protein networks disrupt tissue architecture

(A) Images showing changes in the organization and intensity of Col IV-GFP within the BMs of kinesin mutant egg chambers.

(B) Quantification of mean Col IV-GFP intensity in the BMs from (A). Ordinary one-way ANOVA with Šídák's multiple comparisons test; ns, p > 0.05; *p < 0.05, ****p < 0.0001. In order on graph, n = 16, 10, 16, 11, 10, 10, and 12 egg chambers.

proteins toward the basal surface may provide a general mechanism to ensure that BM assembly and cellular rearrangements can coincide within a tissue.

STAR★METHODS

Detailed methods are provided in the online version of this paper and include the following:

- KEY RESOURCES TABLE
- RESOURCE AVAILABILITY
  - Lead contact
  - Materials availability
  - Data and code availability
- EXPERIMENTAL MODEL AND SUBJECT DETAILS
  - *Drosophila* care
- METHOD DETAILS
  - Generation of *Khc-73³⁻³* allele
  - Egg chamber dissections
  - Live imaging sample preparation
  - Extracellular stain of Col IV-GFP
  - Immunostaining
  - smiFISH
  - Mounting fixed samples
  - Microscopy
  - Quantification of lateral BM proteins
  - Quantification of extracellular lateral Col IV-GFP
  - Quantification of apical BM proteins
  - Line-scans of β-catenin and Col IV-GFP
  - Colocalization of Col IV-GFP and the ER
  - Quantification of YFP-Rab10
  - Quantification of the effect of HA-Khc-73 OE
  - Live imaging YFP-Rab10 in HA-Khc-73 OE cells
  - Live imaging and tracking of YFP-Rab10
  - Quantification of apical and basal YFP-Rab10 levels
  - Measurement of fraction of Col IV within BM fibrils
  - Color 3D projections
  - 3D projections of intercellular Col IV-GFP
  - smiFISH quantification
  - Quantification of Patronin-GFP
  - Quantification of Jupiter-GFP
  - Quantification of YFP-Patronin and γTub23C-eGFP
  - Quantification of EB1 dynamics
  - Generation of Videos
- QUANTIFICATION AND STATISTICAL ANALYSIS

SUPPLEMENTAL INFORMATION

Supplemental information can be found online at https://doi.org/10.1016/j.cub.2021.12.025.

REFERENCES

1. Jayadev, R., and Sherwood, D.R. (2017). Basement membranes. Curr. Biol. *27*, R207–R211.

2. Ramos-Lewis, W., and Page-McCaw, A. (2019). Basement membrane mechanics shape development: lesson from the fly. Matrix Biol *75–76*, 72–81.

3. Randles, M.J., Humphries, M.J., and Lennon, R. (2017). Proteomic definitions of basement membrane composition in health and disease. Matrix Biol *57–58*, 12–28.

4. Funk, S.D., Lin, M.-H., and Miner, J.H. (2018). Alport syndrome and Pierson syndrome: diseases of the glomerular basement membrane. Matrix Biol *71–72*, 250–261.

5. Has, C., and Nyström, A. (2015). Epidermal basement membrane in health and disease. Curr. Top. Membr. *76*, 117–170.

6. Mao, M., Alavi, M.V., Labelle-Dumais, C., and Gould, D.B. (2015). Type IV collagens and basement membrane diseases: cell biology and pathogenic mechanisms. Curr. Top. Membr. *76*, 61–116.

7. Yurchenco, P.D., McKee, K.K., Reinhard, J.R., and Rüegg, M.A. (2018). Laminin-deficient muscular dystrophy: molecular pathogenesis and structural repair strategies. Matrix Biol *71–72*, 174–187.

8. Rodriguez-Boulan, E., and Macara, I.G. (2014). Organization and execution of the epithelial polarity programme. Nat. Rev. Mol. Cell Biol. *15*, 225–242.

9. Kreitzer, G., Schmoranzer, J., Low, S.H., Li, X., Gan, Y., Weimbs, T., Simon, S.M., and Rodriguez-Boulan, E. (2003). Three-dimensional

(C) 3D projections of Col IV-GFP intercellular networks in *Khc-73³⁻³* and *Khc^RNAi^* & *Khc-73^RNAi^* epithelia, and an apical web-like network in a *Khc^RNAi^* & *Khc-73³⁻³* epithelium. Planes containing the BM were removed before making projection. View looks down on apical surface.

(D) Quantification of the fraction of Col IV-GFP intensity associated with BM fibrils in (A). One-way ANOVA followed by Dunn's multiple comparison test; ns, p > 0.05; ****p < 0.0001. For control and *Khc-73³⁻³* (gray region of graph), unpaired t test, ***p < 0.0005. In order on graph, n = 16, 9, 16, 11, 10, and 10 egg chambers.

(E) Images showing Col IV-GFP intercellular cables affect cell and nuclear shapes. A color height projection of Col IV-GFP from a confocal volume of the full thickness of the epithelium shows ectopic cables of Col IV-GFP coincide with deformed cells and nuclei (germ cell nuclei manually removed). White arrows indicate where intercellular Col IV cables contact the BM, and green arrows highlight deformed nuclei (3D projection of 1 deformed nucleus in inset). Images oriented with migration down.

Stage 8. Data represent mean ± SD, plotted on a log scale (B). Scale bars, 10 μm. See also Video S6.

analysis of post-Golgi carrier exocytosis in epithelial cells. Nat. Cell Biol. *5*, 126–136.

10. Ahmed, S.M., and Macara, I.G. (2017). The Par3 polarity protein is an exocyst receptor essential for mammary cell survival. Nat. Commun. *8*, 14867.

11. Polishchuk, R., Di Pentima, A.D., and Lippincott-Schwartz, J. (2004). Delivery of raft-associated, GPI-anchored proteins to the apical surface of polarized MDCK cells by a transcytotic pathway. Nat. Cell Biol. *6*, 297–307.

12. Hua, W., Sheff, D., Toomre, D., and Mellman, I. (2006). Vectorial insertion of apical and basolateral membrane proteins in polarized epithelial cells revealed by quantitative 3D live cell imaging. J. Cell Biol. *172*, 1035–1044.

13. Farr, G.A., Hull, M., Mellman, I., and Caplan, M.J. (2009). Membrane proteins follow multiple pathways to the basolateral cell surface in polarized epithelial cells. J. Cell Biol. *186*, 269–282.

14. Caplan, M.J., Stow, J.L., Newman, A.P., Madri, J., Anderson, H.C., Farquhar, M.G., Palade, G.E., and Jamieson, J.D. (1987). Dependence on pH of polarized sorting of secreted proteins. Nature *329*, 632–635.

15. Boll, W., Partin, J.S., Katz, A.I., Caplan, M.J., and Jamieson, J.D. (1991). Distinct pathways for basolateral targeting of membrane and secretory proteins in polarized epithelial cells. Proc. Natl. Acad. Sci. USA *88*, 8592–8596.

16. De Almeida, J.B., and Stow, J.L. (1991). Disruption of microtubules alters polarity of basement membrane proteoglycan secretion in epithelial cells. Am. J. Physiol. *261*, C691–C700.

17. Bacallao, R., Antony, C., Dotti, C., Karsenti, E., Stelzer, E.H., and Simons, K. (1989). The subcellular organization of Madin-Darby canine kidney cells during the formation of a polarized epithelium. J. Cell Biol. *109*, 2817–2832.

18. Mogensen, M.M., Tucker, J.B., and Stebbings, H. (1989). Microtubule polarities indicate that nucleation and capture of microtubules occurs at cell surfaces in Drosophila. J. Cell Biol. *108*, 1445–1452.

19. Toya, M., Kobayashi, S., Kawasaki, M., Shioi, G., Kaneko, M., Ishiuchi, T., Misaki, K., Meng, W., and Takeichi, M. (2016). CAMSAP3 orients the apical-to-basal polarity of microtubule arrays in epithelial cells. Proc. Natl. Acad. Sci. USA *113*, 332–337.

20. Noordstra, I., Liu, Q., Nijenhuis, W., Hua, S., Jiang, K., Baars, M., Remmelzwaal, S., Martin, M., Kapitein, L.C., and Akhmanova, A. (2016). Control of apico–basal epithelial polarity by the microtubule minus-end-binding protein CAMSAP3 and spectraplakin ACF7. J. Cell Sci. *129*, 4278–4288.

21. Nashchekin, D., Fernandes, A.R., and St Johnston, D. (2016). Patronin/Shot cortical foci assemble the noncentrosomal microtubule array that specifies the Drosophila anterior-posterior axis. Dev. Cell *38*, 61–72.

22. Khanal, I., Elbediwy, A., Diaz de la Loza, M.D.C., Fletcher, G.C., and Thompson, B.J. (2016). Shot and Patronin polarise microtubules to direct membrane traffic and biogenesis of microvilli in epithelia. J. Cell Sci. *129*, 2651–2659.

23. Horne-Badovinac, S., and Bilder, D. (2005). Mass transit: epithelial morphogenesis in the Drosophila egg chamber. Dev. Dyn. *232*, 559–574.

24. Denef, N., Chen, Y., Weeks, S.D., Barcelo, G., and Schüpbach, T. (2008). Crag regulates epithelial architecture and polarized deposition of basement membrane proteins in Drosophila. Dev. Cell *14*, 354–364.

25. Lerner, D.W., McCoy, D., Isabella, A.J., Mahowald, A.P., Gerlach, G.F., Chaudhry, T.A., and Horne-Badovinac, S. (2013). A Rab10-dependent mechanism for polarized basement membrane secretion during organ morphogenesis. Dev. Cell *24*, 159–168.

26. Devergne, O., Sun, G.H., and Schüpbach, T. (2017). Stratum, a homolog of the human GEF Mss4, partnered with Rab8, controls the basal restriction of basement membrane proteins in epithelial cells. Cell Rep *18*, 1831–1839.

27. Isabella, A.J., and Horne-Badovinac, S. (2016). Rab10-mediated secretion synergizes with tissue movement to build a polarized basement membrane architecture for organ morphogenesis. Dev. Cell *38*, 47–60.

28. Gutzeit, H.O. (1991). Organization and in vitro activity of microfilament bundles associated with the basement membrane of Drosophila follicles. Acta Histochem. Suppl. *41*, 201–210.

29. Haigo, S.L., and Bilder, D. (2011). Global tissue revolutions in a morphogenetic movement controlling elongation. Science *331*, 1071–1074.

30. Crest, J., Diz-Muñoz, A., Chen, D.-Y., Fletcher, D.A., and Bilder, D. (2017). Organ sculpting by patterned extracellular matrix stiffness. Elife *6*, e24958.

31. Viktorinová, I., and Dahmann, C. (2013). Microtubule polarity predicts direction of egg chamber rotation in Drosophila. Curr. Biol. *23*, 1472–1477.

32. Chen, D.-Y., Lipari, K.R., Dehghan, Y., Streichan, S.J., and Bilder, D. (2016). Symmetry breaking in an edgeless epithelium by Fat2-regulated microtubule polarity. Cell Rep *15*, 1125–1133.

33. Sherwood, N.T., Sun, Q., Xue, M., Zhang, B., and Zinn, K. (2004). Drosophila Spastin regulates synaptic microtubule networks and is required for normal motor function. PLoS Biol *2*, e429.

34. Buszczak, M., Paterno, S., Lighthouse, D., Bachman, J., Planck, J., Owen, S., Skora, A.D., Nystul, T.G., Ohlstein, B., Allen, A., et al. (2007). The carnegie protein trap library: a versatile tool for Drosophila developmental studies. Genetics *175*, 1505–1531.

35. Liao, E.H., Gray, L., Tsurudome, K., El-Mounzer, W.E., Elazzouzi, F., Baim, C., Farzin, S., Calderon, M.R., Kauwe, G., and Haghighi, A.P. (2018). Kinesin Khc-73/KIF13B modulates retrograde BMP signaling by influencing endosomal dynamics at the Drosophila neuromuscular junction. PLoS Genet *14*, e1007184.

36. Devergne, O., Tsung, K., Barcelo, G., and Schüpbach, T. (2014). Polarized deposition of basement membrane proteins depends on phosphatidylinositol synthase and the levels of phosphatidylinositol 4,5-bisphosphate. Proc. Natl. Acad. Sci. USA *111*, 7689–7694.

37. Mahowald, A.P. (1972). Ultrastructural observations on oogenesis in Drosophila. J. Morphol. *137*, 29–48.

38. Genova, J.L., and Fehon, R.G. (2003). Neuroglian, Gliotactin, and the Na+/K+ ATPase are essential for septate junction function in Drosophila. J. Cell Biol. *161*, 979–989.

39. Isasti-Sanchez, J., Münz-Zeise, F., Lancino, M., and Luschnig, S. (2021). Transient opening of tricellular vertices controls paracellular transport through the follicle epithelium during Drosophila oogenesis. Dev. Cell *56*, 1083–1099.e5.

40. Siddiqui, N., and Straube, A. (2017). Intracellular cargo transport by kinesin-3 motors. Biochemistry (Mosc) *82*, 803–815.

41. Kreitzer, G., and Myat, M.M. (2018). Microtubule motors in establishment of epithelial cell polarity. Cold Spring Harb. Perspect. Biol. *10*, a027896.

42. Stenmark, H. (2009). Rab GTPases as coordinators of vesicle traffic. Nat. Rev. Mol. Cell Biol. *10*, 513–525.

43. Deng, C.-Y., Lei, W.-L., Xu, X.-H., Ju, X.-C., Liu, Y., and Luo, Z.-G. (2014). JIP1 mediates anterograde transport of Rab10 cargos during neuronal polarization. J. Neurosci. *34*, 1710–1723.

44. Zou, W., Yadav, S., DeVault, L., Jan, Y.N., and Sherwood, D.R. (2015). RAB-10-Dependent membrane transport is required for dendrite arborization. PLoS Genet *11*, e1005484.

45. Chen, Y., Wang, Y., Zhang, J., Deng, Y., Jiang, L., Song, E., Wu, X.S., Hammer, J.A., Xu, T., and Lippincott-Schwartz, J. (2012). Rab10 and myosin-Va mediate insulin-stimulated GLUT4 storage vesicle translocation in adipocytes. J. Cell Biol. *198*, 545–560.

46. Schuck, S., Gerl, M.J., Ang, A., Manninen, A., Keller, P., Mellman, I., and Simons, K. (2007). Rab10 is involved in basolateral transport in polarized Madin–Darby canine kidney cells. Traffic *8*, 47–60.

47. Etoh, K., and Fukuda, M. (2019). Rab10 regulates tubular endosome formation through KIF13A/B motors. J. Cell Sci. *132*, jcs226977.

48. Gillingham, A.K., Bertram, J., Begum, F., and Munro, S. (2019). In vivo identification of GTPase interactors by mitochondrial relocalization and proximity biotinylation. eLife *8*, e45916.

49. Clark, I.E., Jan, L.Y., and Jan, Y.N. (1997). Reciprocal localization of Nod and kinesin fusion proteins indicates microtubule polarity in the Drosophila oocyte, epithelium, neuron and muscle. Development *124*, 461–470.

50. Hancock, W.O. (2014). Bidirectional cargo transport: moving beyond tug of war. Nat. Rev. Mol. Cell Biol. *15*, 615–628.

51. Brendza, K.M., Rose, D.J., Gilbert, S.P., and Saxton, W.M. (1999). Lethal kinesin mutations reveal amino acids important for ATPase activation and structural coupling. J. Biol. Chem. *274*, 31506–31514.

52. Kamal, A., and Goldstein, L.S.B. (2002). Principles of cargo attachment to cytoplasmic motor proteins. Curr. Opin. Cell Biol. *14*, 63–68.

53. Burute, M., and Kapitein, L.C. (2019). Cellular logistics: unraveling the interplay between microtubule organization and intracellular transport. Annu. Rev. Cell Dev. Biol. *35*, 29–54.

54. Jolly, A.L., Kim, H., Srinivasan, D., Lakonishok, M., Larson, A.G., and Gelfand, V.I. (2010). Kinesin-1 heavy chain mediates microtubule sliding to drive changes in cell shape. Proc. Natl. Acad. Sci. USA *107*, 12151–12156.

55. Winding, M., Kelliher, M.T., Lu, W., Wildonger, J., and Gelfand, V.I. (2016). Role of kinesin-1–based microtubule sliding in Drosophila nervous system development. Proc. Natl. Acad. Sci. USA *113*, E4985–E4994.

56. Stoops, E.H., Hull, M., Olesen, C., Mistry, K., Harder, J.L., Rivera-Molina, F., Toomre, D., and Caplan, M.J. (2015). The periciliary ring in polarized epithelial cells is a hot spot for delivery of the apical protein gp135. J. Cell Biol. *211*, 287–294.

57. Nekrasova, O.E., Amargo, E.V., Smith, W.O., Chen, J., Kreitzer, G.E., and Green, K.J. (2011). Desmosomal cadherins utilize distinct kinesins for assembly into desmosomes. J. Cell Biol. *195*, 1185–1203.

58. Matis, M., Russler-Germain, D.A., Hu, Q., Tomlin, C.J., and Axelrod, J.D. (2014). Microtubules provide directional information for core PCP function. eLife *3*, e02893.

59. Serra-Marques, A., Martin, M., Katrukha, E.A., Grigoriev, I., Peeters, C.A., Liu, Q., Hooikaas, P.J., Yao, Y., Solianova, V., Smal, I., et al. (2020). Concerted action of kinesins KIF5B and KIF13B promotes efficient secretory vesicle transport to microtubule plus ends. eLife *9*, e61302.

60. Guardia, C.M., Farías, G.G., Jia, R., Pu, J., and Bonifacino, J.S. (2016). BORC functions upstream of kinesins 1 and 3 to coordinate regional movement of lysosomes along different microtubule tracks. Cell Rep *17*, 1950–1961.

61. Zahavi, E.E., Hummel, J.J.A., Han, Y., Bar, C., Stucchi, R., Altelaar, M., and Hoogenraad, C.C. (2021). Combined kinesin-1 and kinesin-3 activity drives axonal trafficking of TrkB receptors in Rab6 carriers. Dev. Cell *56*, 494–508.e7.

62. Soppina, V., Norris, S.R., Dizaji, A.S., Kortus, M., Veatch, S., Peckham, M., and Verhey, K.J. (2014). Dimerization of mammalian kinesin-3 motors results in superprocessive motion. Proc. Natl. Acad. Sci. USA *111*, 5562–5567.

63. Arpağ, G., Norris, S.R., Mousavi, S.I., Soppina, V., Verhey, K.J., Hancock, W.O., and Tüzel, E. (2019). Motor dynamics underlying cargo transport by pairs of Kinesin-1 and Kinesin-3 motors. Biophys. J. *116*, 1115–1126.

64. Cerqueira Campos, F.C., Dennis, C., Alégot, H., Fritsch, C., Isabella, A., Pouchin, P., Bardot, O., Horne-Badovinac, S., and Mirouse, V. (2020). Oriented basement membrane fibrils provide a memory for F-actin planar polarization via the dystrophin-dystroglycan complex during tissue elongation. Development *147*, dev186957.

65. Walma, D.A.C., and Yamada, K.M. (2020). The extracellular matrix in development. Development *147*, dev175596.

66. Morin, X., Daneman, R., Zavortink, M., and Chia, W. (2001). A protein trap strategy to detect GFP-tagged proteins expressed from their endogenous loci in Drosophila. Proc. Natl. Acad. Sci. USA *98*, 15050–15055.

67. Kohrs, F.E., Daumann, I.-M., Pavlovic, B., Jin, E.J., Kiral, F.R., Lin, S.-C., Port, F., Wolfenberg, H., Mathejczyk, T.F., Linneweber, G.A., et al. (2021). Systematic functional analysis of Rab GTPases reveals limits of neuronal robustness to environmental challenges in flies. eLife *10*, e59594.

68. Sarov, M., Barz, C., Jambor, H., Hein, M.Y., Schmied, C., Suchold, D., Stender, B., Janosch, S., K J, V.V., Krishnan, R.T., et al. (2016). A genome-wide resource for the analysis of protein localisation in Drosophila. eLife *5*, e12068.

69. Zhang, J., Schulze, K.L., Hiesinger, P.R., Suyama, K., Wang, S., Fish, M., Acar, M., Hoskins, R.A., Bellen, H.J., and Scott, M.P. (2007). Thirty-one flavors of Drosophila Rab proteins. Genetics *176*, 1307–1322.

70. Dunst, S., Kazimiers, T., von Zadow, F., Jambor, H., Sagner, A., Brankatschk, B., Mahmoud, A., Spannl, S., Tomancak, P., Eaton, S., and Brankatschk, M. (2015). Endogenously tagged Rab proteins: a resource to study membrane trafficking in Drosophila. Dev. Cell *33*, 351–365.

71. Lu, W., Fox, P., Lakonishok, M., Davidson, M.W., and Gelfand, V.I. (2013). Initial neurite outgrowth in Drosophila neurons is driven by kinesin-powered microtubule sliding. Curr. Biol. *23*, 1018–1023.

72. Siegrist, S.E., and Doe, C.Q. (2005). Microtubule-induced pins/Galphai cortical polarity in Drosophila neuroblasts. Cell *123*, 1323–1335.

73. Wang, H., Brust-Mascher, I., Civelekoglu-Scholey, G., and Scholey, J.M. (2013). Patronin mediates a switch from kinesin-13–dependent poleward flux to anaphase B spindle elongation. J. Cell Biol. *203*, 35–46.

74. Mukherjee, A., Brooks, P.S., Bernard, F., Guichet, A., and Conduit, P.T. (2020). Microtubules originate asymmetrically at the somatic Golgi and are guided via Kinesin2 to maintain polarity within neurons. eLife *9*, e58943.

75. Shimada, Y., Yonemura, S., Ohkura, H., Strutt, D., and Uemura, T. (2006). Polarized transport of frizzled along the planar microtubule arrays in Drosophila wing epithelium. Dev. Cell *10*, 209–222.

76. Gratz, S.J., Cummings, A.M., Nguyen, J.N., Hamm, D.C., Donohue, L.K., Harrison, M.M., Wildonger, J., and O'Connor-Giles, K.M. (2013). Genome engineering of Drosophila with the CRISPR RNA-guided Cas9 nuclease. Genetics *194*, 1029–1035.

77. Schindelin, J., Arganda-Carreras, I., Frise, E., Kaynig, V., Longair, M., Pietzsch, T., Preibisch, S., Rueden, C., Saalfeld, S., Schmid, B., et al. (2012). Fiji: an open-source platform for biological-image analysis. Nat. Methods *9*, 676–682.

78. Li, Y., and Munro, E. (2021). Filament-guided filament assembly provides structural memory of filament alignment during cytokinesis. Dev. Cell *56*, 2486–2500.e6.

79. Gratz, S.J., Ukken, F.P., Rubinstein, C.D., Thiede, G., Donohue, L.K., Cummings, A.M., and O'Connor-Giles, K.M. (2014). Highly specific and efficient CRISPR/Cas9-catalyzed homology-directed repair in Drosophila. Genetics *196*, 961–971.

80. Cetera, M., Lewellyn, L., and Horne-Badovinac, S. (2016). Cultivation and live imaging of Drosophila ovaries. Methods Mol. Biol. *1478*, 215–226.

81. Doerflinger, H., Benton, R., Shulman, J.M., and St Johnston, D.S. (2003). The role of PAR-1 in regulating the polarised microtubule cytoskeleton in the Drosophila follicular epithelium. Development *130*, 3965–3975.

82. Tsanov, N., Samacoits, A., Chouaib, R., Traboulsi, A.-M., Gostan, T., Weber, C., Zimmer, C., Zibara, K., Walter, T., Peter, M., et al. (2016). smiFISH and FISH-quant – a flexible single RNA detection approach with super-resolution capability. Nucleic Acids Res *44*, e165.

83. Lord, S.J., Velle, K.B., Mullins, R.D., and Fritz-Laylin, L.K. (2020). SuperPlots: communicating reproducibility and variability in cell biology. J. Cell Biol. *219*, e202001064.

84. Skora, A.D., and Spradling, A.C. (2010). Epigenetic stability increases extensively during Drosophila follicle stem cell differentiation. Proc. Natl. Acad. Sci. USA *107*, 7389–7394.

85. Lee, M.-C., and Spradling, A.C. (2014). The progenitor state is maintained by lysine-specific demethylase 1-mediated epigenetic plasticity during Drosophila follicle cell development. Genes Dev *28*, 2739–2749.

86. Lee, M.-C., Skora, A.D., and Spradling, A.C. (2017). Identification of genes mediating Drosophila follicle cell progenitor differentiation by screening for modifiers of GAL4::UAS variegation. G3 (Bethesda) *7*, 309–318.

87. Aurich, F., and Dahmann, C. (2016). A mutation in fat2 uncouples tissue elongation from global tissue rotation. Cell Rep *14*, 2503–2510.

88. Gonzalez, R.C., and Woods, R.E. (2017). Digital Image Processing, Fourth Edition (Pearson).

STAR★METHODS

KEY RESOURCES TABLE

REAGENT or RESOURCE	SOURCE	IDENTIFIER
Antibodies		
anti-Discs large	Developmental Studies Hybridoma Bank	Cat# DHSB: 4F3; RRID: AB_528203
anti-aPKC	Santa Cruz Biotechnology	Cat# sc-216; RRID: AB_2300359
anti-Armadillo (β-catenin)	Developmental Studies Hybridoma Bank	Cat# DHSB: N2 7A1; RRID: AB_528089
GFP-Booster Alexa Fluor 647	ChromoTek	Cat# gb2AF647-50; RRID: AB_2827575
Anti-acetylated α-Tubulin (6-11B-1)	Santa Cruz Biotechnology	Cat# sc-23950; RRID: AB_628409
Anti-Notch	Developmental Studies Hybridoma Bank	Cat# DHSB: C458.2H; RRID: AB_528408
anti-Fasciclin III	Developmental Studies Hybridoma Bank	Cat# DHSB: 7G10; RRID: AB_528238
Anti-Tango1	Lerner et al.[25]	N/A
Anti-GM130 (Drosophila)	Abcam	Cat# ab30637; RRID: AB_732675
Rabbit polyclonal anti-HA	Rockland	Cat# 600-401-384; RRID: AB_218007
Alexa Fluor 555, donkey anti-mouse secondary	Thermo Fisher Scientific	Cat# A31570; RRID: AB_2536180
Alexa Fluor 647, donkey anti-mouse secondary	Thermo Fisher Scientific	Cat# A31571; RRID: AB_162542
Alexa Fluor 555, donkey anti-rabbit secondary	Thermo Fisher Scientific	Cat# A-31572; RRID: AB_162543
Alexa Fluor 647, donkey anti-rabbit secondary	Thermo Fisher Scientific	Cat# A31573; RRID: AB_2536183
Alexa Fluor 647, goat anti-guinea pig secondary	Thermo Fisher Scientific	Cat# A-21450; RRID: AB_2735091
Chemicals, peptides, and recombinant proteins		
Alexa Fluor 647 phalloidin	Thermo Fisher Scientific	Cat# A22287
CellMask Deep Red Plasma Membrane Stain	Thermo Fisher Scientific	Cat# C10046
CellMask Orange Plasma Membrane Stain	Thermo Fisher Scientific	Cat# C10045
Schneider's Drosophila Medium	Thermo Fisher Scientific	Cat# 21720-024
Fetal Bovine Serum	Gibco	Cat# 10438-018
Recombinant Human Insulin	Millipore Sigma	Cat# 12643
Soda Lime Glass Beads, 48-51 μm	Cospheric LLC	Cat# S-SLGMS-2.5
Formaldehyde, 16%, methanol free, Ultra Pure	Polysciences	Cat# 18814-10
VECTASHIELD Antifade Mounting Medium	Vector Laboratories	Cat# H-1000-10
SlowFade Antifade Kit	Thermo Fisher Scientific	Cat# S2828
Experimental models: Organisms/strains		
D. melanogaster. Standard control strain: w[1118]	Bloomington Drosophila Stock Center	BDSC: 3605; FlyBase ID: FBst0003605
D. melanogaster. traffic jam-Gal4: y* w*; P{w+mW.hs = GawB}NP1624/CyO, P{w- = UAS-lacZ.UW14}UW14	Kyoto Stock Center	DGRC: 104055; FlyBase ID: FBst0302922
D. melanogaster. w[1118]; P{w[+mC] = UAS-Dcr-2.D}10	Bloomington Drosophila Stock Center	BDSC: 24651; FlyBase ID: FBst0024651
D. melanogaster. P{ry[+t7.2] = hsFLP}22, w[*]}	Bloomington Drosophila Stock Center	BDSC: 8862; FlyBase ID: FBst0008862
D. melanogaster. Col IV-GFP: P{PTT-GC}vkg[CC00791]	Buszczak et al.[34]; Morin et al.[66]	FlyBase ID: FBal0211825
D. melanogaster. w1118; Khc-73 [3-3]	This paper	N/A

Continued

REAGENT or RESOURCE	SOURCE	IDENTIFIER
D. melanogaster. w[*]; P{w[+mW.hs] =FRT(w[hs])}G13	Bloomington Drosophila Stock Center	BDSC: 1956
D. melanogaster. rab10-	Kohrs et al.[67]	N/A
D. melanogaster. Rab10[RNAi]: y[1] v[1]; P{y[+t7.7] v[+t1.8]=TRiP.JF02058}attP2	Bloomington Drosophila Stock Center	BDSC: 26289; FlyBase ID: FBtp0040618
D. melanogaster. UAS-spastin	Sherwood et al.[33]	FlyBase ID: FBal0177735
D. melanogaster. PBac{ LanA-GFP[fTR000 574.sfGFP-TVPTBF]}VK00033	Vienna Drosophila Resource Collection[68]	VDRC: 318155; FlyBase ID: FBal0339089
D. melanogaster. Khc-73[RNAi]: y[1] sc[*] v[1] sev[21]; P{y[+t7.7] v[+t1.8] =TRiP.HMS01624}attP40	Bloomington Drosophila Stock Center	BDSC: 36733; FlyBase ID: FBal0266531
D. melanogaster. Perlecan-GFP: P{PTT-GA}trolCA06698	Buszczak et al.[34]; Morin et al.[66]	FlyBase ID: FBal0282690
D. melanogaster. Khc-73[149]	Liao et al.[35]	FlyBase ID: FBal0344596
D. melanogaster. hsFLP; FRTG13 Ubi-mRFP.nls/Cyo	From the laboratory of Dan T. Bergstralh	N/A
D. melanogaster. traffic jam-Gal4 FRTG13 UbimRFP.nls: w[*];P{w+mW.hs = GawB}NP1624 P{w[+mW.hs]=FRT(w[hs])}G13 P{w[+mC]=Ubi-mRFP.nls}2R	Recombination only, this paper	traffic jam-Gal4 from DGRC: 104055; FRTG13 from BDSC: 1956; Ubi-mRFP.nls from BDSC: 35496
D. melanogaster. vkg-GFP traffic jam-Gal4 FRTG13 UbimRFP.nls: w[*];P{PTT-GC} vkg[CC00791] P{w+mW.hs = GawB}NP1624 P{w[+mW.hs]=FRT(w[hs])}G13 P{w[+mC] =Ubi-mRFP.nls}2R	Recombination only, this paper	vkg-GFP from FlyBase ID: FBti0099948; traffic jam-Gal4 from DGRC: 104055; FRTG13 from BDSC: 1956; Ubi-mRFP.nls from BDSC: 35496
D. melanogaster. y[1] w[*]; P{w[+mC] =UASp-YFP.Rab10}21	Bloomington Drosophila Stock Center[69]	BDSC: 9789; FlyBase ID: FBal0215407
D. melanogaster. w[*]; P{w[+mC]=UAS-ChRFP-Tub}2	Bloomington Drosophila Stock Center	BDSC: 25774; FlyBase ID: FBst0025774
D. melanogaster. w[1118] TI{TI}Rab10 [EYFP]	Bloomington Drosophila Stock Center[70]	BDSC: 62548; FlyBaseID: FBst0062548
D. melanogaster. Ubi-Jupiter-mCherry (III)	Lu et al.[71]	FlyBase ID: FBtp0085844
D. melanogaster. UAS-RFP-Rab10 (II)	Isabella and Horne-Badovinac[27]	N/A
D. melanogaster. PBac{Khc-73[fTRG01377].sfGFP-TVPTBF} VK00033	Vienna Drosophila Resource Collection[68]	VDRC: 318350; FlyBase ID: FBal0339158
D. melanogaster. P{UASt-Khc-73.HA} (III)	Seigrist and Doe[72]	FlyBase ID: FBal0193854
D. melanogaster. w1118; PBac{602.P.SVS-1}Pdi[CPTI000688]	Vienna Drosophila Resource Collection	VDRC: 115041; FlyBase ID: FBal0262348
D. melanogaster. w[*]; P{w[+mC]=Ubi-p63E-Patronin.A.GFP}3M/TM3, Sb[1]	Bloomington Drosophila Stock Center[73]	BDSC: 55129; FlyBase ID: FBal0290910
D. melanogaster. w[1118]; P{w[+mC]=PTT-GA}Jupiter[G00147].	Morin et al.[66]	BDSC:6836; FlyBase ID: FBal0148245
D. melanogaster. Klc[RNAi]: y[1] sc[*] v[1] sev [21]; P{y[+t7.7] v[+t1.8]=TRiP.HMS00883} attP2	Bloomington Drosophila Stock Center	BDSC: 33934; FlyBase ID: FBal0257559
D. melanogaster. Khc[RNAi] : y[1] sc[*] v[1] sev [21]; P{y[+t7.7] v[+t1.8]=TRiP.GL00330} attP2	Bloomington Drosophila Stock Center	BDSC: 35409; FlyBase ID: FBal0262797
D. melanogaster. w[*];P{w[+mW.hs]=FRT (w[hs])}G13 Khc27/Cyo	Brendza et al.[51]	FlyBase ID: FBal0101625
D. melanogaster. w[*];P{w[+mW.hs]=FRT (w[hs])}G13 TI{TI}KhcKO.mutA/Cyo	Winding et al.[55]	BDSC: 79036; FlyBase ID: FBal0326706
D. melanogaster. w[*]; P{w[+mC]=UASp-RFP.KDEL}10/TM3, Sb[1]	Bloomington Drosophila Stock Center	BDSC: 30909; FlyBase ID: FBst0030909
D. melanogaster. YFP-Patronin	Nashchekin et al.[21]	N/A

(Continued on next page)

Continued

REAGENT or RESOURCE	SOURCE	IDENTIFIER
D. melanogaster. γ-Tubulin at 23C-eGFP/Cyo	Mukherjee et al.[74]	N/A
D. melanogaster. Ubi-EB1-GFP (III)	Shimada et al.[75]	FlyBase ID: FBal0216831
Oligonucleotides		
Fwd primer for chiRNA plasmid in exon 3 of Khc-73: 5'-CTTCGATATGCACGCATTATAGCCC-3'	This paper	N/A
Rev primer for chiRNA plasmid in exon 3 of Khc-73: 5'-AAACGGGCTATAATGCGTGCATATC-3'	This paper	N/A
Fwd primer for chiRNA plasmid in exon 4 of Khc-73: 5'-CTTCGCTTGTACATAAGCTCGGGTG-3'	This paper	N/A
Rev primer for chiRNA plasmid in exon 4 of Khc-73: 5'-AAACCACCCGAGCTTATGTACAAGC-3'	This paper	N/A
Fwd primer used to sequence lesion in Khc-73[3-3]: 5'-CAACCAAAGACATTCGCATTC-3'	This paper	N/A
Rev primer used to sequence lesion in Khc-73[3-3]: 5'-GATGTTAGAGCCTTCCTTGAG-3'	This paper	N/A
smiFISH probe sequences are listed in Methods S1	This paper	N/A
Recombinant DNA		
Plasmid: pU6-BbsI-chiRNA	Gratz et al.[76]	Addgene plasmid # 45946; RRID: Addgene_45946
Plasmid: pU6 guide Khc-73 exon 3	This paper	N/A
Plasmid: pU6 guide Khc-73 exon 4	This paper	N/A
Software and algorithms		
Fiji	Schindelin et al.[77]	https://fiji.sc
HandBrake 1.3.3 The open source video transcoder	HandBrake Team	https://handbrake.fr/
Zen Blue	Zeiss	https://www.zeiss.com/microscopy/us/products/microscope-software/zen.html
Zen Black	Zeiss	https://www.zeiss.com/microscopy/us/products/microscope-software/zen.html
MetaMorph	Molecular Devices	https://www.moleculardevices.com/products/cellular-imaging-systems/acquisition-and-analysis-software/metamorph-microscopy#gref
MATLAB R2020a	MathWorks	https://www.mathworks.com/products/matlab.html
MATLAB Sobel operator	Li and Munro[78]	N/A
Prism8 and Prism9 for MacOS	GraphPad Software, LLC	https://www.graphpad.com/scientific-software/prism/
Microsoft Excel for Mac, version 16.45	Microsoft	https://www.microsoft.com/en-us/microsoft-365/excel

RESOURCE AVAILABILITY

Lead contact

Further information and requests for resources and reagents should be directed to and will be fulfilled by the Lead Contact, Sally Horne-Badovinac (shorne@uchicago.edu).

Materials availability

New *Drosophila* lines and plasmids generated in this study are available by request to the Lead Contact above.

Data and code availability

- All data reported in this paper will be shared by the Lead Contact upon request.
- This study did not generate new code.
- Any further information needed to reanalyze the data reported in this paper is available from the Lead Contact upon request.

EXPERIMENTAL MODEL AND SUBJECT DETAILS

Drosophila care

Drosophila melanogaster were reared on cornmeal molasses agar food at 25°C using standard techniques. The genotypes used in each experiment are listed in Methods S1, indexed by figure panel. Females were aged on yeast with males prior to dissection; temperatures and yeasting conditions used for each experiment are in Methods S1, indexed by figure panel.

METHOD DETAILS

Generation of *Khc-73³⁻³* allele

Clustered regularly interspaced short palindromic repeats (CRISPR) genome editing was used to induce a lesion near the amino-terminus of Khc-73 within the motor domain. Two guide RNAs were selected using *Drosophila* RNAi Screening Center's "Find CRISPRs" on-line tool, one within exon 3 (5' ATATGCACGCATTATAGCCC**TGG** 3') and one within exon 4 (5' CTTGTACAT AAGCTCGGGTG**TGG** 3'). The PAM motifs are in bold. The underlined sequences were cloned into pU6-BbsI-chiRNA following the methods in Gratz et al.[76,79] and the website flycrispr.org. *GenetiVision* injected chiRNA plasmids into embryos expressing nanos-Cas9 from the x chromosome. Individual lines were established and screened by PCR and sequencing. The *Khc-73³⁻³* allele has a lesion near only the guide site in exon 3 that results in a change to 5 amino acids followed by an early stop codon. Amino acids 92-97 within exon 3 in wild-type Khc-73 are YNACIF, with a nucleotide sequence of 5'-TATAATGCGTGCATATTC-3'. In *Khc-73³⁻³* the nucleotide sequence is 5'-TTACGGCCAGACAGGTGA-3' and results in an early stop codon(*) LRPDR*. We focus on developmental stages 7 and 8 in this mutant because there are not obvious defects in BM protein secretion earlier in development with loss of only Khc-73. BM protein secretion is highest at stage 7, which could make it easier to detect secretion defects, but we cannot rule out developmental changes in secretion regulation.

Egg chamber dissections

Ovaries were removed from yeasted females using 1 set of Dumont #55 forceps and 1 set of Dumont #5 forceps in live cell imaging media in a spot plate (Schneider's *Drosophila* medium containing 1X Penicillin-Streptomycin, 15% fetal bovine serum, and 200 μg/ml insulin). Ovariole strands were mechanically removed from muscle with forceps. Egg chambers older than stage 9 were cut away from the ovariole strand in the stalk region using a 27-gauge needle. For additional methods and videos of dissection, see Cetera et al.[80]

Live imaging sample preparation

For live imaging, dissected ovarioles were quickly moved to a fresh well of live imaging media in a spot plate. In some live experiments, noted in the appropriate sections, CellMask Orange or Deep Red plasma membrane stain was used to visualize cell edges and aid in imaging setup. Either version of CellMask was added at 1:2000 to ovarioles in live imaging media for 10 min. The ovarioles were then washed 2x in fresh live imaging media to remove excess stain. To make a live imaging slide, 1-5 ovarioles were transferred to a glass slide in 10 μl of live imaging media. Glass beads (between 10 and 50) with a mean diameter of 51 μm were added for use as spacers, and arranged around the egg chambers using an eyelash tool. A 10 μl drop of fresh live imaging media was added to a #1.5 22x22 mm square cover glass to prevent bubbles, and slowly lowered onto the egg chambers. The slide was sealed with melted petroleum jelly before imaging. New dissections were done ~every hour to avoid artifacts arising from extended *ex vivo* culture.

Extracellular stain of Col IV-GFP

Egg chambers were fixed for 6 min at RT in 4% EM grade formaldehyde in phosphate buffered saline (PBS), washed 3x5 min in PBS at RT, and stained with 1:2000 anti-GFP nanobody conjugated to Alexa Fluor 647 (GFP-Booster) and 4′,6-diamidino-2-phenylindole (DAPI) for 15 min at RT with rocking *without* permeabilization to allow the nanobody access to only the extracellular pool of Col IV-GFP. Samples were washed 3x5 min with PBS.

Immunostaining

Egg chambers were fixed in 4% EM-grade formaldehyde in PBS with 0.1% Triton X-100 (PBST) for permeabilization for 15 min at RT, and then washed 3x10 min in PBST. For microtubule (MT) staining, 8% formaldehyde in PBST was used to better preserve MTs.[81]

Egg chambers were incubated with primary antibodies diluted in PBST overnight at 4°C with rocking. Primary antibody dilutions: aPKC (1:100), Dlg (1:10), Tango1 (1:1000), GM130 (1:500), acetylated α-tubulin (1:100), Armadillo (1:100), Notch (1:100), HA (1: 500). Egg chambers were washed from primary antibody 3x10 min in PBST with rocking at RT. Secondary antibodies were diluted 1:500 in PBST and incubated with egg chambers for 3 hrs at RT with rocking, followed by washing 3x10 min in PBST.

smiFISH

Single molecule inexpensive fluorescent *in situ* hybridization (smiFISH) was based on Tsanov et al.[82] and protocols provided by Matt Ronshaugen's lab. In this technique, DNA probes specific to the mRNA of interest are fused to a "flap" sequence that will anneal to a complementary, fluorescently-labeled "flap" sequence to allow visualization of the mRNA.

Probe design and annealing

DNA probes specific to *col41a* mRNA (based on cDNA clone RE33133) were designed using LGC Biosearch Technologies' Stellaris RNA FISH Probe Designer with the following settings: probe length 20 bases, masking level 5, minimal spacing 2 bases. 48 probes were ordered for *col4a1*. Each probe contained 20 nucleotides complementary to the mRNA for *col4a1* with Flap-X (5'CCTC CTAAGTTTCGAGCTGGACTCAGTG 3') appended to the 3' end. Probes were ordered from Integrated DNA Technologies (IDT) as 100 µM stocks in Tris-EDTA, pH 8.0 (TE) in a 96-well plate. Probes were mixed at equal molar ratios to make a stock of unlabeled probes and stored at -20°C. Working stocks were diluted 5-fold in TE buffer before use. Fluorescently labeled Flap-X binding probes were ordered from IDT as DNA oligos with 5' and 3' Cy5 modifications and resuspended in TE at 100 µM. All probe sequences are listed in Methods S1. Probes for *col4a1* and fluorescent probes were annealed immediately before use by mixing: 2 µl of *col4a1* probe set, 0.5 µl of 100 µM Cy5-FlapX, 1 µl of New England Biolabs Buffer 3, and 6.5 µl water. A PCR machine was used to incubate mixtures at 85°C for 3 min, 65°C for 3 min, and 25°C for 5 min.

Hybridization

Egg chambers were fixed in 4% EM-grade formaldehyde in PBST for 15 min at RT and washed 3x5 min in PBST. Egg chambers were exchanged into a 1:1 mixture of PBST and smiFISH wash buffer [5 ml 20X SSC (0.3M sodium citrate, 3M NaCl, pH7.0), 5 ml deionized formamide, 40 ml nuclease-free water] and incubated at RT for 10 min. Egg chambers were washed 2x in smiFISH wash buffer, followed by a final incubation of 30 min at 37°C. smiFISH hybridization buffer (1 g dextran sulfate, 1 ml 20x SSC, 1 ml deinionzed form-amide, 7.5 ml nuclease-free water) was warmed to 37°C. Egg chambers were incubated with a mixture of 10 µl of annealed probes in 500 µl of smiFISH hybridization buffer at 37°C for 16 hrs protected from light. To wash, 500 µl of smiFISH wash buffer was added to dilute hybridization buffer and the egg chambers were spun briefly in a table-top micro-centrifuge to pellet them. Egg chambers were washed 3x10 min at 37°C in 500 µl of smiFISH wash buffer. This was followed by incubating at RT in a 1:1 dilution of smiFISH wash buffer with PBST, followed by one 10 min incubation in PBST containing DAPI and Alexa Fluor 488 Phalloidin, followed by 2x10 min washes with PBST at RT.

Mounting fixed samples

For all types of fixed samples, the majority of buffer was removed from samples and they were mounted in ~35 µl SlowFade antifade or VECTASHIELD on a slide with a #1.5 22x50 mm coverslip, sealed with nail polish, and stored at 4°C prior to imaging.

Microscopy

Fixed and live laser scanning confocal imaging

Imaging was performed on a Zeiss LSM 800 laser scanning confocal microscope run by Zen Blue with a 63x Plan A apochromat 1.4NA oil objective. Live imaging was performed at RT. Used in Figures 1D, 1F, 1G, 2A–2C, 2E, 3A, 3B, 4A–4D, 5A, 5C, 5D, 5F, 6A–6D, 7A–7E, S1A, S1B, S1D–S1F, S2A, S2B, S2D, S3A, S3B, S3F, S3G, S4A–S4G, S5A–S5D, S6A, S6B, and S6D, and Videos S1 and S6.

Airyscan fixed imaging

Imaging was performed on a Zeiss LSM 880 laser scanning confocal microscope with Airyscan and a 63x Plan A apochromat 1.4NA oil objective, run by Zen Black. Used in Figures 3D, 3E, S4H, and S6E, and Videos S2 and S5.

Live spinning disk confocal and partial TIRF imaging

Imaging was performed on a Nikon Ti-E inverted microscope equipped with solid-state 50 mW 481 and 561 nm Sapphire lasers (Coherent), a Yokogawa CSU-X1 spinning-disk scan head, and an Andor iXon3 897 electron-multiplying charged-coupled device (EM-CCD) cameras run by MetaMorph software. When using the TIRF microscope, we adjusted the laser below the critical angle to illuminate a thicker region of the sample (partial TIRF). Live imaging was performed at RT. Spinning disk used in Figures 3G and 3G' and Video S3. Partial TIRF used in Figures 3C, 4F–4H, S3C–S3E, S4I, S5C, S6F–S6H, and S7B–S7D and Videos S4 and S5.

Quantification of lateral BM proteins

Single confocal images were taken in a plane through the lateral domains, near the apical surfaces of follicle cells from late stage 8 egg chambers when new Col IV-GFP synthesis is low and ectopic lateral Col IV-GFP in mutant egg chambers is easily visible. The average intensity of Col IV-GFP associated with lateral domains was measured by segmenting the lateral domains based on anti-Dlg staining. In Fiji, Dlg images were processed as follows: background was subtracted with Rolling Ball Background Subtraction with a radius of 10 pixels, Threshold was used to create a binary mask, Despeckle was used to remove noise, Dilate was used to fill in gaps in the lateral edges, Skeletonize was used to reduce the mask to a one pixel outline, and finally Dilate was used to reach a uniform line

thickness of 0.7 μm. This binary mask was used to measure the mean intensity of Col IV-GFP within only the lateral regions. In some images, the Dlg staining quality was too noisy for automatic segmentation, and the cell edges were manually traced in Fiji and converted to the same thickness as the automatic segmentation. For LanA-GFP and Perlecan-GFP, samples were counterstained with Alexa Fluor 647 Phalloidin, not anti-Dlg. F-actin highlights the cell edges, which were manually traced in Fiji and then converted to the same line thickness as the automatic segmentation. The data were normalized to the mean of the control egg chambers for easy comparison as fold-change relative to control. The control and $Khc-73^{3-3}$ egg chamber data is used in both Figure 1 and again in Figure 5 for comparison to $Khc-73^{3-3}$ & Khc^{RNAi} since all experimental conditions were the same.

Quantification of extracellular lateral Col IV-GFP

Extracellular Col IV staining is necessary during stages when new Col IV protein synthesis is high (stage 7 in these experiments) and Col IV-GFP foci are scattered throughout the cytoplasm, obscuring the secreted, lateral Col IV-GFP population. Three planes were chosen from a confocal z-stack of mosaic $Khc-73^{3-3}$ tissue for analysis: a plane "near basal", or about 1 μm above the BM, a plane through the middle of the cell ("mid-cell"), and a plane just below the apical surface of cells ("near-apical"). The lateral cell edges were manually traced in Fiji with a line thickness of 1.12 μm at each z-plane. The mean intensity of the anti-GFP nanobody staining (extracellular Col IV-GFP, see Figure S1F) was measured in the segmented lateral regions for both the control and $Khc-73^{3-3}$ cell regions. Additional background subtraction was required to quantify lateral extracellular Col IV-GFP because the "near basal" plane is near the BM, which creates high background fluorescence. Therefore, the mean intensity was also measured in the inverse regions, within the cell centers where there should not be any extracellular staining; the mean intensity in these cell center regions was used for background subtraction in each plane. The background-corrected mean lateral intensity is calculated: mean intensity lateral regions – mean intensity central regions. To allow the data to be read as fold change between control and $Khc-73^{3-3}$ cells in one egg chamber, and be compared across z-planes, all data was divided by the mean of the control cells in the "near basal" images for each egg chamber.

Quantification of apical BM proteins

In images of cross-sections through egg chambers expressing Col IV-GFP and stained for aPKC to mark the apical domain, lines of 0.74 μm thickness were manually drawn along the apical surface by tracing the anti-aPKC signal, and the mean Col IV intensity within this line was measured. Since lateral Col IV accumulates just under the ZA in Khc-73 mutant tissue (Figures 2A and 2B), which is very close to the apical surface, drawing this line does also include some of this lateral signal. However, this measurement captures the dramatic increase in apical Col IV in conditions such as $Rab10^{RNAi}$ or Khc^{RNAi} & $Khc-73^{3-3}$ (Figures 5A–5C). Data were normalized to the mean of the control data.

Line-scans of β-catenin and Col IV-GFP

Confocal cross-sectional images were taken through control and $Khc-73^{3-3}$ egg chambers expressing Col IV-GFP and stained for β-catenin. In Fiji, lines of 0.58 μm thickness were manually drawn along cell-cell junctions starting above the apical surface and extending along the lateral domain. The average intensities of Col IV-GFP and β-catenin were measured along the line-scan using Plot Profile in Fiji and exported to Microsoft Excel. The maximum intensity of β-catenin was used to determine the location of the zonulae adherentes and used as a comparison point to align all the traces; ZA were set to a distance of zero. All individual traces for Col IV-GFP intensity were plotted to show the range of accumulation patterns. β-catenin is drawn as a line at zero as it is used only as a spatial reference point for the ZA.

Colocalization of Col IV-GFP and the ER

Egg chambers expressing UAS-RFP-KDEL as a luminal marker of the ER and Col IV-GFP were dissected and stained with CellMask Deep Red as described. Egg chambers were imaged live to better preserve ER structure. For the images shown, three consecutive frames from a time-lapse taken 1 sec apart were averaged to decrease noise.

Quantification of YFP-Rab10

At basal trailing cell edges

Images were taken along the basal surface of cells in mosaic tissues. YFP-Rab10 is present as a diffuse cytoplasmic signal as well as a more intense signal on puncta and tubules at basal trailing cell edges, likely representing the vesicular structures of interest. To focus our measurements on the YFP-Rab10 associated with these putative vesicular structures, we quantified YFP-Rab10 intensity changes in only basal trailing cell edges so that the mean YFP-Rab10 measurements would not be dominated by the cytoplasmic signal that covers a much larger area of cells. In Fiji, a line with a thickness of 1.2 μm was manually drawn along the back of each cell and the mean YFP-Rab10 intensity was measured in each cell. To normalize the YFP-Rab10 intensities across egg chambers, the entire control cell area was manually segmented in Fiji and the mean YFP-Rab10 intensity measured. All individual cell values were divided by this value. In addition to individual cell measurements, we also calculated the mean of all cells per genotype for each egg chamber. Statistical tests were performed using these mean egg chamber values, but all individual cells are also plotted to show the variability in the underlying data.[83]

Near the ERES

YFP-Rab10 is localized near ERES/Golgi regions throughout the volume of the cells. Near the basal surface, the tubules at the backs of cells are brighter than the signal by the Golgi, and their close, and sometimes overlapping, signals makes it difficult to measure the

levels of YFP-Rab10 near ERES/Golgi. In the middle of the cells, the majority of the YFP-Rab10 is concentrated near the ERES/Golgi so we chose this plane to allow easier segmentation. Tango1 staining at the ERES was used to segment these regions with the following steps: Rolling Ball Background Subtraction with radius 10 pixels was used, Threshold was used to create a binary mask of the ERES, and noise was removed by running Despeckle 2x in Fiji. The ERES was expanded using Dilate 2x so it would encompass the region adjacent to the ERES where Rab10 is normally found. The mean intensity of YFP-Rab10 within these ERES masks was measured in both the control cells and $Khc-73^{3-3}$ cells in each mosaic egg chamber, resulting in a single mean value per genotype per egg chamber. Since the same mosaic egg chambers were also used to measure the basal trailing edge YFP-Rab10 intensity, just at different z-planes, these ERES means were normalized using the same value used to normalize YFP-Rab10 at the basal trailing edge between egg chambers.

Quantification of the effect of HA-Khc-73 OE
We used the *traffic jam-Gal4* (*tj-Gal4*) driver to express UAS-HA-Khc73.[72] The *tj-Gal4* driver usually expresses UAS transgenes in all follicle cells, but some UAS transgenes in our experience express in only a subset of cells, which we refer to as "patchy" expression in the text. We do not know why UAS-HA-Khc-73 in particular expresses in this patchy way. This phenomenon has also been described as variegation in expression in follicle cells, thought to stem from epigenetic changes.[84–86] Since we can stain for the HA epitope tag, we were able to select non-expressing, "control" cells and HA-Khc-73 expressing cells. Images were taken near the basal surface of tissues patchily overexpressing HA-Khc-73, which clusters at the basal trailing edges of cells. To determine if HA-Khc-73 recruited other proteins to these clusters, we measured intensities in 1.2 μm lines drawn along the basal trailing edges of cells, similar to the procedure used to measure basal trailing edge YFP-Rab10 intensity. We chose to measure along the trailing edges instead of segmenting the HA+ regions because this more general location could be selected in the non-expressing cells as a control for baseline localization of candidate proteins to the trailing edge of cells. Cells that were negative for HA-Khc-73 staining ("control") or positive for HA-Khc-73 were selected from within the same egg chamber. The mean intensity of the relevant endogenously-tagged, fluorescently-labeled protein (YFP-Rab10, Col IV-GFP, PDI-GFP (ER), or anti-GM130 (cis Golgi) staining) was measured for each cell. For each egg chamber, all individual cell measurements were normalized by dividing by the mean value for control cells within that egg chamber. In addition to individual cell measurements, we also calculated the mean of all cells per group ("control" or "HA-Khc-73") for each egg chamber. Statistical tests were performed using these mean group values, but all individual cells are also plotted to show the variability in the underlying data.[83]

Live imaging YFP-Rab10 in HA-Khc-73 OE cells
We used the *traffic jam-Gal4* (*tj-Gal4*) driver to express UAS-HA-Khc73 and UAS-YFP-Rab10. Images were collected using partial TIRF in a continuous 200 ms stream to follow the rapid movements of YFP-Rab10.

Live imaging and tracking of YFP-Rab10
Selection of egg chambers
In some experiments, CellMask Orange plasma membrane stain was used to visualize cell edges. To ensure egg chambers were not damaged during dissection or sample preparation, we first determined if they were migrating at a normal rate. A 5-30 min time-lapse using 300 ms exposures taken every 15 sec was taken for each egg chamber to ensure it was migrating at a normal speed (a cutoff of > 0.4 μm/min was set for the stage 7 egg chambers used). Sets of control and $Khc-73^{3-3}$ egg chambers were always imaged in the same session to prevent biases from day-to-day variability in live imaging conditions. Since partial TIRF imaging was used, there is uneven illumination across the field of cells.
Tracking and analysis
To allow tracking of rapidly moving individual YFP-Rab10 puncta, time-lapse videos with 300 ms exposures captured every 1 sec for 2 min were made. YFP-Rab10 puncta were manually tracked using the Manual Tracking plugin in Fiji. All puncta that moved at least 3 pixels (0.3 μm) per 1 sec time-step over at least 3 consecutive frames were tracked in at least 5 cells per egg chamber to obtain a minimum of 50 tracks per egg chamber, in 5 egg chambers per genotype. We sometimes observed a change in direction of a YFP-Rab10 punctum. Each segment in a single direction was counted as a separate "run", allowing a single punctum to represent multiple runs. Each run was scored by eye for its overall direction, either towards the trailing or leading edge of the cell. For each egg chamber, the number of tracks moving towards the trailing edge of the cell was divided by the number of tracks moving towards the leading edge of each cell, such that a value greater than 1 indicates a bias in movement towards the trailing edge where YFP-Rab10 accumulates. The control data is included in the text of the results as a single ratio and in Figure 4. In addition, the speed of each "run" was calculated. Speed was calculated as the Euclidian frame-to-frame displacement. All individual "run" speeds across all 5 egg chambers were plotted to compare the distributions between control and $Khc-73^{3-3}$ cells, and the mean speed per egg chamber was also plotted and used for statistical comparison between genotypes. All analysis was done on original images; for display in figures, images were rotated in Fiji so that the direction of cell migration is toward the bottom of the page.
Editing of images for Video S5
For videos, images were rotated such that the direction of cell migration is toward the bottom of the page. The CellMask staining channel was processed with a Rolling Ball Background subtraction, radius 20, in Fiji. Both the YFP-Rab10 and CellMask channels were processed with Bleach Correction in Fiji for the first segment of Video S5. The images of trajectories were generated in Fiji with the Manual Tracking plug-in.

Quantification of apical and basal YFP-Rab10 levels

In images of cross-sections through egg chambers, lines of 0.6 μm thickness were manually drawn along the basal surface and apical surface of the follicular epithelium of each egg chamber, and the mean intensity of YFP-Rab10 was measured in Fiji. The ratio of the apical and basal surface values was calculated for each egg chamber, such that a ratio greater than 1 indicates an enrichment of YFP-Rab10 on the apical surface, and a ratio less than 1 indicates an enrichment of YFP-Rab10 on the basal surface.

Measurement of fraction of Col IV within BM fibrils

As a way to quantify changes in the organization of Col IV-GFP within the BM, we measured the fraction of Col IV-GFP intensity associated with fibril-like structures in the BMs of different genotypes. We have previously performed this analysis and refer to it as "fibril fraction."[27] First, we determined if the overall mean intensity of Col IV-GFP was the same. The mean intensity of Col IV-GFP in a confocal plane though the BM was measured in a square region (3600 μm^2) for each egg chamber in Fiji. The genotype that causes apical secretion had significantly reduced Col IV-GFP in the BM, so it was excluded from fibril fraction analysis. To segment the fibrils, the median intensity of Col IV-GFP was measured for each egg chamber and a threshold of 1.35x median intensity was used to threshold and define the brighter, "fibril" areas. The Col IV-GFP intensity in these "fibril" regions was divided by the total Col IV-GFP intensity in the image to obtain the % of total Col IV-GFP intensity associated with fibrils.

Color 3D projections
Of MTs

The temporal color-code plug-in in Fiji was used to generate a color z-projection of an Airyscan confocal z-stack of MTs. An antibody specific to acetylated MTs was used for this imaging because this antibody has been used in all previous work characterizing the basal MTs in follicle cells[31,32,87] and we wanted to ensure we visualized the same MTs as past work. Live imaging of MTs labeled with UAS-ChRFP-Tubulin or Jupiter-GFP show a similar organization of MTs at the basal surface (Figures 3G and S3C).

Of intercellular BM protein network

The temporal color-code plug-in in Fiji was used to generate a color z-projection of Col IV-GFP in a confocal z-stack through the full-thickness of the follicle cells (9 μm). The cell outlines are Dlg staining of lateral cell edges in a single plane through the middle of FCs. The nuclei are maximum intensity projections of the DAPI signal from the z-stack to show the full shape of the nucleus. In the more apical slices of the z-stack, the large nuclei from the germline nurse cells were visible; these were manually circled and deleted from the z-stack prior to making the maximum intensity projection. The 3D projection of a deformed nucleus was generated with Clear-Volume in Fiji.

3D projections of intercellular Col IV-GFP

A 3D confocal z-stack through the full thickness of the follicle cells was collected. The slices containing the BM were deleted to provide better contrast to visualize the intercellular Col IV-GFP network. 3D projections were generated in Fiji using the Plugin ClearVolume.

smiFISH quantification

The density of *col4a1* mRNA precluded single-molecule counting. We used the intensity of the smiFISH probes as a proxy for mRNA levels. Three z-planes through the lateral domains of the follicle cells were chosen for analysis in each egg chamber to determine if the localization of mRNA changed in mutant cells: a plane along the basal surface, a plane through the mid-section of the cells, and a plane near the apical surface. Within the mosaic tissue, regions encompassing cells of different genotypes were manually drawn based on the nuclear clone marker in Fiji. The mean intensity of *col4a1* mRNA was measured for each genotype at each plane. Intensities in different genotypes within mosaic tissues were compared within the same egg chamber at each plane by: dividing *Khc-73³⁻³* cells by control cells, or dividing *Khc^RNAi* & *Khc-73³⁻³* cells by *Khc^RNAi* only cells. The direction of follicle cell migration (to orient images) was determined by the organization of F-actin rich leading edges along the basal surface visualized by counterstaining egg chambers with Alexa Fluor 488 Phalloidin.

Quantification of Patronin-GFP

Egg chambers were fixed and stained with Alexa Fluor 647 Phalloidin and DAPI. Confocal cross-sections were taken through egg chambers. In Fiji, a 1.1 μm thick line was manually drawn along the apical surface where Patronin is normally enriched,[21,22] using the F-actin stain to visualize cell outlines. The mean apical intensity of Ubi-PatroninA-GFP in *Khc-73³⁻³* cells was divided by that of control cells in each egg chamber, resulting in a ratio of 1 when there is no change.

Quantification of Jupiter-GFP
Intensity in cross-section

Confocal cross-sections were taken through live egg chambers stained with CellMask Deep Red plasma membrane stain to identify the edges of cells. In Fiji, the control and *Khc-73³⁻³* cells were manually outlined based on the clone marker, and the mean intensity of endogenously-tagged Jupiter-GFP (a MT-associated protein) was measured as a proxy for MT mass. The mean Jupiter-GFP intensity in *Khc-73³⁻³* cells was divided by that of the control cells in each egg chamber.

Basal MT alignment

Partial TIRF images of the basal surface of live mosaic egg chambers expressing Jupiter-GFP were taken. First, a 5-30 min time-lapse was collected to determine the direction of migration, and to exclude non-migratory egg chambers damaged during dissection. To quantify MT alignment, we used an approach based on the Sobel operator[88] to identify the sharp local gradients in fluorescent intensity present orthogonal to linear structures like MTs, as implemented in Li and Munro.[78] Images of Jupiter-GFP were convolved with the following 3x3 kernel Sobel operators to measure the x and y components of the fluorescent intensity gradient (Gx and Gy, respectively).

$$Gx = \begin{matrix} 1 & 2 & 1 \\ 0 & 0 & 0 \\ -1 & -2 & -1 \end{matrix} \quad \text{and} \quad Gy = \begin{matrix} 1 & 0 & -1 \\ 2 & 0 & -2 \\ 1 & 0 & -1 \end{matrix}$$

For each pixel, the angle and magnitude of the gradient can be calculated using the x and y components of the gradient. Since the gradient is orthogonal to the angle of the MT, the angle of the MTs, θ, is

$$\theta = \tan^{-1}\frac{Gy}{Gx}$$

And the magnitude of the gradient, G, is

$$G = \sqrt{Gx^2 + Gy^2}$$

To create MT alignment distributions, regions of cells with different genotypes were manually outlined in Fiji based on the clone marker. The pixels within regions of a given genotype were binned by angle with weight G, collapsed to 0°-90° since we do not take into account angle relative to the A-P axis, and then normalized to 100%. The mean ± SD at each angle bin of all egg chambers of a given genotype were plotted on a rose diagram, where perfect alignment with the direction of migration would be 90° and alignment orthogonal to migration would be 0°. To statistically compare the amount of alignment between genotypes, the % of the alignment histogram within 60°-90° was used as a proxy measurement of the population of "highly aligned MTs". This "% highly aligned MTs" measurement was performed for each genotype in each egg chamber. All analysis was done on original images; for display in figures, images were rotated so that the direction of cell migration is toward the bottom of the page. MT intensity appears uneven across the egg chamber because these images were collected with partial TIRF which creates an uneven illumination depth and some interference patterns across the imaging field.

Quantification of YFP-Patronin and γTub23C-eGFP

Confocal cross-sections of egg chambers expressing endogenously-tagged YFP-Patronin[21] or γTub23C-eGFP[74] were collected. In Fiji, 5 lines with width 4 μm were manually drawn through the apical-basal axis and the mean intensity profile exported to Excel (avoiding apical centrosomes). The line-scans were aligned by the position of the apical surface. The mean intensity of the apical and basal regions, defined as the 1.2 μm regions at the top and bottom of the cells, was calculated and normalized to the mean intensity across the whole cell. The major enrichment of γTub23C-eGFP was at the 2 apically localized centrosomes. To report this enrichment, we selected a confocal image through the apical plane and manually circled 20 centrosomes per egg chamber and measured the mean intensity of γTub23C-eGFP in centrosomes and normalized it to the mean intensity in the surrounding cytoplasm.

Quantification of EB1 dynamics

Time-lapse videos of egg chambers expressing Ubi-EB1-GFP and stained with CellMask Orange were taken at the basal surface using near TIRF. First, 5 min videos of cell edges labeled with CellMask were taken at a rate of 1 frame per 15 sec to determine the direction of migration. Ubi-EB1-GFP dynamics were imaged at 1 frame per 1 sec for 2-5 min. The direction of all Ubi-EB1-GFP+ comets was scored manually in Fiji as "towards the trailing edge" or "towards the leading edge" over a 100 sec time-lapse in a 198 μm^2 area. To measure the dynamics of EB1-GFP along the apical-basal axis, time-lapse videos of egg chambers in cross-section were taken with Zeiss Airyscan at 1 frame per sec. The direction of Ubi-EB1-GFP+ comets was scored manually as "towards the basal surface" or "towards the apical surface" in a 120 sec video that contained ∼6 cells. The EB1-GFP comets grow densely along the apical surface, and these were excluded from analysis.

Generation of Videos

Fiji was used to add labels and export videos as .avi, which were then converted to .mp4 using HandBrake.

QUANTIFICATION AND STATISTICAL ANALYSIS

Egg chambers with visible damage from dissection or dying cells, or not migrating at a normal speed in live imaging experiments, were excluded. All experiments were replicated at least once. All statistical tests were performed in Prism8 or Prism9. MATLAB and Microsoft Excel were used as indicated in STAR Method Details for some data analysis. All data was tested for normality using the Shapiro-Wilks test and a non-parametric statistical test was chosen if a dataset was not normal. For comparisons between cells with different genetic perturbations within a mosaic tissue, a paired statistical test was chosen. When experiments compared data taken from different egg chambers, unpaired statistical tests were used. One-way ANOVA followed by a multiple comparisons test

was used for comparison of more than two datasets. Many experiments compare the ratio between mutant and control cells within a mosaic tissue, which would result in a value of 1 if there was no difference between groups; in these experiments a one-sample t-test or the non-parametric Wilcoxon signed rank test was used to compare the experimental ratio to the theoretical value of 1expected for no change between genotypes. The number of biological replicates (n), specific statistical tests performed, and significance for each experiment can be found in the figure legends.